REVIEW

Recent strategies for activating the basal planes of transition metal dichalcogenides towards hydrogen production

Hang Xia,[†][a] Zude Shi,[†][a] Chengshi Gong[ab] and Yongmin He [ID] *[a]

The hydrogen evolution reaction (HER) presents an environmentally friendly, efficient, and cost-effective way to produce hydrogen fuel. Recently, two-dimensional (2D) transition metal dichalcogenides (TMDCs) have emerged as a fascinating class of HER materials. Their atomically thin nature acts as an interface with the possibility of maximum exposure of nearly all active sites to the reaction environment. However, for most non-metallic TMDCs, as exemplified by 2H-MoS_2, 1T-$PtSe_2$, and 1T'-$ReSe_2$, their basal planes are usually HER-inert except for minor edges. Based on their rich chemistry, significant progress has been recently made to activate the basal planes for HER. This review provides an overview of the current activating strategies. They can be classified into internal and external regulations, depending on whether the pristine structure is altered or not. The former directly creates more active sites through doping, vacancies, phases, grain boundaries (GBs), and superlattices. On the other hand, the latter indirectly promotes the activity utilizing external methods such as the electric field, strain, substrates, and heterostructures. We discuss each strategy's principles and characteristics and highlight their enhanced catalytic activities. We finally provide personal perspectives on the challenges and opportunities in this emerging field, including a joint strategy, a phase-engineering strategy, electrical–electrocatalytic coupling, as well as the potential of "single-atom-layer" catalysis.

[a]*State Key Laboratory of Chemo/Biosensing and Chemometrics, College of Chemistry and Chemical Engineering, Hunan University, Changsha 410082, P. R. China. E-mail: ymhe@hnu.edu.cn*

[b]*School of Electronic Engineering, Lanzhou City University, Lanzhou 730070, P. R. China*

† Hang Xia and Zude Shi contributed equally to this work.

1. Introduction

Exploring clean and renewable alternative energy technology is highly desirable to alleviate global warming and the environmental degradation caused by the excessive use of non-renewable fossil fuels.[1,2] Electrochemical water splitting that converts electrical energy into hydrogen energy through the hydrogen evolution reaction (HER) is considered a promising green energy technology, exhibiting high energy density, environmental friendliness, and high product purity.[3,4] Platinum

Hang Xia received his B.S. degree in 2019 from Central South University. He is currently a PhD candidate in physical chemistry at Hunan University under the supervision of Professor Yongmin He. His research focuses on micro/nano electrocatalysis for water splitting.

Zude Shi received his M.S. degree in 2021 from Lanzhou University and his B.S. degree in 2018 from the same university. Subsequently, he joined the Yongmin He group at the College of Chemistry and Chemical Engineering, Hunan University, China. His research focuses on the surface and interface electrocatalysis of low-dimensional materials.

This journal is © The Royal Society of Chemistry 2022

J. Mater. Chem. A, 2022, **10**, 19067–19089 | **19067**

(Pt) and other noble metal-based electrocatalysts give superior performance for HER;[5–8] however, their scarcity and poor durability seriously hinder their large-scale application towards hydrogen production.[9–11] Therefore, exploring cheap and efficient HER catalysts as an alternative to noble metals has attracted growing attention. In particular, two-dimensional (2D) transition metal dichalcogenides (TMDCs), represented by MoS_2, are widely favored due to their low cost, layered structures, and fascinating electronic properties.[12–14] To date, substantial research efforts have been devoted to developing highly efficient HER catalysts based on 2D TMDCs. The key advantage is that their atomically thin nature can act as an interface with the possibility of maximum exposure of nearly all active sites to the reaction environment.[15–17]

For a structural point of view, 2D TMDC materials are configured by X–M–X layers (M: transition metal, and X: chalcogen),[18] in which M atoms are sandwiched by two X-atom planes. They have stronger ionic–covalent bonds between M and X atoms in the planes, with weaker van der Waals (vdW) interactions out of the planes. There are two primary structures in a TMDC layer: the basal plane and the edge. Both experiments and theory prove that the basal planes of most non-metallic TMDCs, for example, $2H-MoS_2$, $1T-PtSe_2$, and $1T'-ReSe_2$, are usually catalytically inert in HER, in sharp contrast to the HER-active edges.[19–24] Considering the extremely large area in a TMDC layer (close to 100%),[25,26] activating the inert basal planes presents a promising strategy to improving the overall catalytic activity of a whole layer (Fig. 1).[27] The most intuitive example is that when edge-active $2H-MoS_2$ undergoes a phase transition into basal-plane-active $1T-MoS_2$, the catalytic activity is improved by orders of magnitude.[28–31] Recently, significant progress has been made to activate the basal plane for HER. For example, the HER activity of the MoS_2 basal plane is remarkably boosted by introducing strained vacancies, and its Tafel slope is decreased from 98 mV dec^{-1} to 60 mV dec^{-1}.[32] In another example, an onset potential of −25 mV and Tafel slope of 54 mV dec^{-1} were achieved by activating the MoS_2 basal plane with ultra-high-density grain boundaries (GBs).[33] Based on current

achievements, it is time to offer a critical review of this topic, potentially arousing a wide range of readers for the future development of this field. Note that some excellent reviews have already been published based on 2D TMDCs for HER,[31,34–39] while there is still a lack of summaries focusing only on the basal plane and its activating strategies for HER.

Herein, we summarize currently-developed activating strategies on TMDC basal planes toward hydrogen production (Fig. 2), discuss their principles, and highlight their advantages as well. In brief, we first introduce the HER mechanism in acidic and basic media, emphasizing the critical pH-dependent role of the free energy of hydrogen adsorption (ΔG_{H*}) in the HER process. Then, we classify the strategies into internal or external regulations based on whether the pristine structure has been changed or not. The former is to directly create more active sites in the basal plane, including doping, vacancies, phases, GBs, and superlattices. The latter is to indirectly improve the basal-plane activity through external methods, such as the electric field, strain, substrates, and heterostructures. The underlying principles and characteristics are discussed, and each method presents several representative examples. Finally, we provided personal perspectives on the challenges and opportunities of activating TMDC basal planes to develop high-efficient HER catalysts.

2. HER principle and Gibbs free energy of hydrogen adsorption

There are two possible reaction pathways in the HER process: Volmer–Tafel and Volmer–Heyrovsky mechanisms.[47] Taking the acidic electrolyte as a typical example (Fig. 3a), in the first Volmer step (eqn (1)), the proton obtains an electron on the electrode material (M) surface to generate an adsorbed hydrogen atom (H_{ad}) under the applied external potential. The H_2 products will be generated by the following Tafel step or the Heyrovsky step. In detail, in the Tafel reaction, two neighboring H_{ad} combined on the surface of the electrode to form H_2 (eqn (2)). In contrast, in the Heyrovsky reaction, another proton gets

Dr. Chengshi Gong is an associate professor at Lanzhou City University (China) andis also a visiting scholar in Prof. Yongmin He's research group at Hunan University. Dr. Gong received his PhD Degree in 2014 from Lanzhou University. His research focuses on the preparation of two-dimensional materials and their applications in water splitting.

Dr. Yongmin He is a professor at the College of Chemistry and Chemical Engineering at Hunan University (China). Dr. He obtained his PhD Degree at Lanzhou University in 2015 (China), and later worked in Prof. Zheng Liu and Prof. Qi Jie Wang's groups as a postdoc research fellow (2015–2021) at Nanyang Technological University (Singapore). His research interest focuses on the synthesis and structure-engineering of atom-thin materials, and their electronic or on-chip electrochemical devices, with various applications in nanoelectronics, iontronics, sensors, and electrocatalysis.

Fig. 1 Activating basal planes of two-dimensional (2D) transition metal dichalcogenides (TMDCs). Top: illustration of the activating strategy of the basal planes. Bottom: volcano plot of the exchange current density as a function of the free energy of hydrogen adsorption (ΔG_{H*}) for the original basal planes and the activated ones. Data obtained from ref. 10,19,22,32,40–46 Abbreviations: V-MoS$_2$ for vacancy-MoS$_2$, SV-MoS$_2$ for strained-sulfur vacancy MoS$_2$, WSSe V_s for the S vacancy of WSSe, WSSe V_{se} for the Se vacancy of WSSe, EC for the electric field, and V SAC@1T-WS$_2$ for single-site vanadium substitution in 1T-WS$_2$.

close to the H$_{ad}$ and then receives a new electron to generate H$_2$ (eqn (3)).

$$\text{Volmer step: } H_3O^+ + M + e^- \rightarrow M\text{–}H_{ad} + H_2O \tag{1}$$

$$\text{Tafel step: } 2M\text{–}H_{ad} \rightarrow H_2 + 2M \tag{2}$$

$$\text{Heyrovsky step: } H_3O^+ + M\text{–}H_{ad} + e^- \rightarrow H_2 + M + H_2O \tag{3}$$

No matter, which pathway HER undergoes, the adsorption of hydrogen atoms is a crucial factor. Generally, ΔG_{H*} is recognized as an essential parameter for evaluating the HER performance, and the best HER catalysts possess $\Delta G_{H*} \sim 0$.[48] If ΔG_{H*} is too negative, the conversation and desorption processes will be hindered, easily making the catalyst to be poisoned. On the other hand, a much-positive ΔG_{H*} will weaken the adsorption, leading to inadequate H atoms in the catalytic reaction. A volcano plot is usually used to describe the relationship between ΔG_{H*} and the exchange current density for HER catalysts (Fig. 1). It can be seen that the 2H-MoS$_2$ basal plane, located at the right region of the volcano plots, has a poor H adsorption ability, and its rate-limiting step is the first Volmer step.[22] Once the basal planes of TMDCs are activated to obtain a trade-off between adsorption and desorption, they will be consequently located in the near-central region of the volcano plots.

Notably, both, Volmer–Tafel and Volmer–Heyrovsky's steps are strongly pH-dependent. Distinct from acidic solutions with

sufficient hydronium cations (H$_3$O$^+$) as protons, the proton source in the basic medium (alkaline or neutral) is H$^+$, generated from the water dissociation (Fig. 3b and eqn (4)).[49] As a result, the proton source in basic media is usually limited, and thus leads to a tardy HER rate compared to an acidic solution.[35] Next, for the Tafel step, two H$_{ad}$ directly combined to generate H$_2$ (eqn (5)). For the Heyrovsky step, the H$_{ad}$ would react with H$_2$O and then yields H$_2$ and OH$^-$ (eqn (6)). Note that, except for the above steps, the expense of the water molecules near the electrode surface (*that is*, lowering the water concentration in the electrical double layer) could push the balance of the water-involved reaction (eqn (4) and (6)) in the reverse direction.[50] This phenomenon will further lower the HER rate in the basic medium, on the other hand. Therefore, the rational design of the electrocatalysts with excellent hydrogen adsorption and water dissociation is a vital direction.[51]

$$\text{Volmer step: } H_2O + M + e^- \rightarrow M\text{–}H_{ad} + OH^- \tag{4}$$

$$\text{Tafel step: } 2M\text{–}H_{ad} \rightarrow H_2 + 2M \tag{5}$$

$$\text{Heyrovsky step: } H_2O + M\text{–}H_{ad} + e^- \rightarrow H_2 + OH^- + M \tag{6}$$

3. Internal regulation

This section highlights the recent advances in the internal structural regulation of TMDC's basal planes by engineering

This journal is © The Royal Society of Chemistry 2022

J. Mater. Chem. A, 2022, **10**, 19067–19089 | **19069**

Fig. 2 Overview of the currently-developed strategies for activating TMDC basal planes for the hydrogen evolution reaction (HER). The strategies are divided into internal and external regulation, depending on whether the pristine structure is altered or not. The former is inclined to directly create more active structures, including doping, vacancies, phases, GBs, and superlattices. The latter indirectly promotes the activity of the basal planes by external methods, such as the electric field, strain, substrates, and heterostructures.

their atomic structures, such as metal/nonmetal-doping, vacancies, phases, GBs, and superlattices. These structures would act as the critical active sites in basal planes for HER.

3.1 Doping strategy

3.1.1 Metal-doping of TMDCs. Metal-doping has been widely adopted to activate the basal plane of TMDCs in the HER. Currently, a large number of methods enable effective doping, for example, chemical vapor deposition (CVD),[52–54] solvothermal method,[55,56] electrochemical depositions,[57,58] plasma,[59,60] photoreductions,[61] and self-assembly solution impregnation.[62] According to the atomic structures of the doped metal atoms, this strategy presents two types: substitutional and interstitial doping, as shown in Fig. 4a. For substitutional doping, a large number of transition metals have been reported in TMDCs, such as Co, Fe, V, Cr, Pd, and Re.[63,64] In theory, Tsai et al. used density functional theory (DFT) to calculate the ΔG_{H*} on different species of transition metal-doped MoS_2, providing a rational design of a new MoS_2-type catalyst to strengthen or weaken the binding of key intermediates (Fig. 4b).[55,65,66] However, it was found in the experiments that this doping not only affects the bond strength on doped metal atoms, but also significantly alters their coordination environment that generally introduces SV and local phase transitions of the TMDC

catalysts.[64] For example, Zhou et al. used the CVD approach to make two configurations of metal-doped MoS_2 structures.[67] As shown in Fig. 4c, Fe and Co-based configuration is usually accompanied by the generation of vacancies. Those obtained configurations can greatly improve the HER performance ($3Co_{Mo}$-V_s have the highest performances: a low overpotential at the current density of 10 mA cm^{-2} ($\eta_{10} = 75$ mV vs. RHE), a Tafel slope of 57 mV dec^{-1}, and long-term durability (η_{10} drops by only 10 mV after 1000 cycles)), as shown in Fig. 4d. Similarly, Luo and co-workers obtained substitutional doping of Pd in the MoS_2 basal plane using a solvothermal method, in which SVs were simultaneously introduced to trigger a local phase transition (Fig. 4e). It turned out to be an excellent HER performance approaching Pt/C catalysts (1% Pd–MoS_2 has an exchange current density of 805 μA cm^{-2} and a η_{10} of 78 mV in Fig. 4f).[62] Further, these substituted catalysts with large coordination numbers show excellent structural stability.

On the other hand, interstitial doping, different from the above-mentioned substitution, is located atop the basal plane instead of being confined within the crystal lattice. Currently, Pt, Rh, Pb, Bi, Pd, Sn, Nb, Mo, and Cu[54,57–59] have been used as interstitial dopant atoms in TMDCs for HER. For example, Shi and co-workers obtained a variety of atomically dispersed Pt, Rh, Cu, Pb, Bi, and Sn atoms on the MoS_2 surface using an

19070 | J. Mater. Chem. A, 2022, **10**, 19067–19089

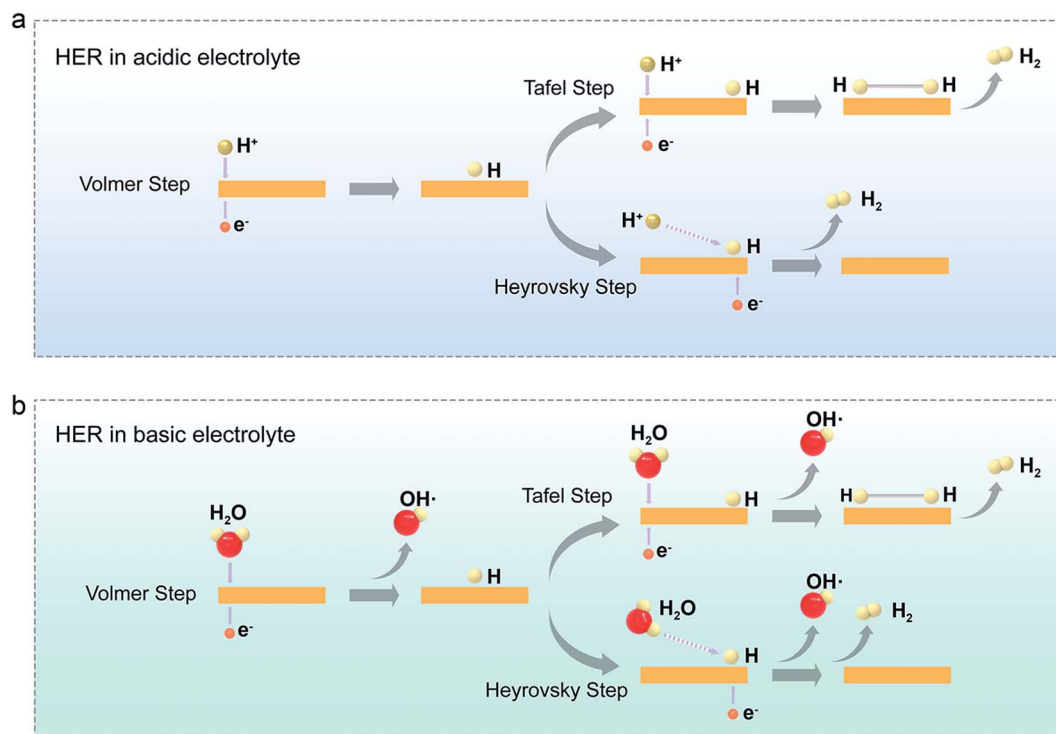This journal is © The Royal Society of Chemistry 2022

Fig. 3 HER mechanism on a TMDC surface in different electrolytes: (a) acidic solution, (b) alkaline or neutral solution. Hydronium cation (H_3O^+) and a water molecule (H_2O) serve as proton donors in the acidic and basic electrolytes, respectively.

electrochemical underpotential deposition (Fig. 4g).[56,58] Later, Yang and co-workers reported interstitial doped 2H-Nb$_{1.35}$S$_2$ using a CVD method, which delivered an exceptionally-high current density in HER (1000 mA cm^{-2} at ~370 mV and 5000 mA cm^{-2} at ~420 mV).[54] In addition to the above heteroatom doping, Luo *et al.* used a cold hydrogen plasma method to synthesize Mo-single-atom doped MoS$_2$ (homo-atom doping), achieving an enhancement of HER activity with a Tafel slope of 36.4 mV dec^{-1} and a high current density of 400 mA cm^{-2} at ~260 mV, as a result of the increase of hydrogen bond strength through hybridization in Fig. 4h.[59]

3.1.2 Nonmetal-doping of TMDCs. It is compelling to see that many workers[59,68–70] have also employed various non-metallic doping of TMDCs to activate their basal planes, such as Se,[71] P,[72] B,[73] F,[74] and N[75] doping. In 2017, Zhao *et al.* comprehensively examined the effect and changes in the band structure of various non-metal doped TMDCs,[76] theoretically providing a suitable non-metallic element for HER (Fig. 5a). Later, Pető and co-workers found that the monolayer MoS$_2$ exposed to the ambient atmosphere at room temperature would undergo an irreversible oxygen-substitution reaction. The oxygen atoms would be dropped into the basal plane to improve the HER performance (Fig. 5b and c).[77] It was also observed that oxygen doping could facilitate expanding the interlayer distance and promote the transfer of protons.[78] In addition to oxygen doping, Zang and co-workers also synthesized carbon (C)-doped MoS$_2$ (Fig. 5d), which turned out to have low overpotential in an alkaline solution, close to that of the commercial Pt/C. The reason is the C-introduced orbital modulation effect, which

generates empty 2p orbitals perpendicular to the basal plane, thus facilitating the adsorption and dissociation of water in alkaline solution, as shown in Fig. 5e.[79] Xiao *et al.* fabricated nitrogen (N)-doped MoS$_2$ using one-step sintering method, which presents a low onset overpotential of 35 mV and Tafel slope of 41 mV dec^{-1}. Those N dopants in MoS$_2$ could extremely increase the number of active sites toward HER and enhance the conductivity of the catalysts as well (Fig. 5g).[75] Interestingly, Janus TMDC materials (MXY, M = transition metal, X/Y = S, Se, or Te, and X ≠ Y)[80] were also reported (Fig. 5f).[81] They gave a better HER performance than the pristine ones, originating from the synergistic effect between the intrinsic defects and inherent structural strain in a Janus structure.[82]

Benefiting from the abundant valence states and flexible oxidation capabilities of these non-metal atoms, their doping method can finely modulate the electronic structure of TMDCs and accelerate and stabilize the HER process. Notably, the co-doping of metals and non-metals has also been tried, which improves the intrinsic performance and increases catalytic sites by alloying and synergy at different sites.[67] As a whole, non-metal doping offers great potential to trigger more TMDCs-based catalyst reconstruction and optimize the reaction pathways.

3.2 Vacancy strategy

Vacancies are the commonly-found structures in TMDCs. Their distribution (isolated vacancies, di-sulfur vacancies, pair vacancies, cluster vacancies, *etc.*), concentration, and species[83]

This journal is © The Royal Society of Chemistry 2022

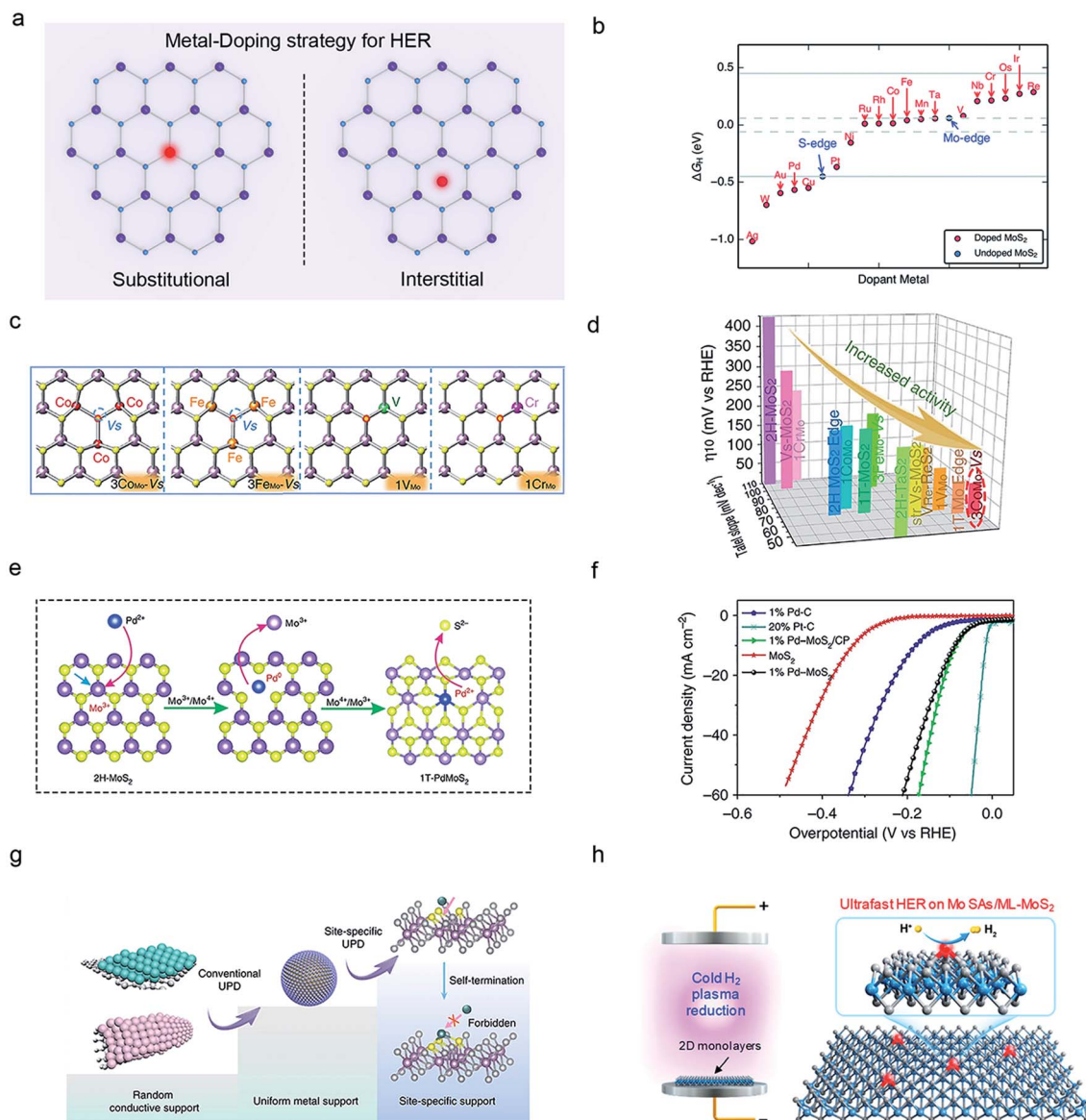*J. Mater. Chem. A*, 2022, **10**, 19067–19089 | **19071**

Fig. 4 Metal-doping strategy of 2D-TMDCs for HER. (a) Schematic illustration of the substitutional (left) and interstitial (right) metal-doping in TMDCs. (b) Range of ΔG_{H*} on each transition metal-doped MoS_2. Reproduced with permission,[65] Royal Society of Chemistry. (c) Two configurations of metal-doped MoS_2 structures, in which the sulfur vacancies (SVs) are marked in blue circles and the H-bonded S atoms in red circles. (d) The corresponding η_{10}-Tafel slope in 0.5 M H_2SO_4 for the HER catalysts in (c). Reproduced with permission,[67] Springer Nature. Substitutional doping of Pd in the MoS_2 basal plane (e) and the polarization curves of the resultant catalysts (f). Reproduced with permission,[62] Springer Nature. (g) Schematic illustration of the single-atom doping on the TMDC surfaces through an electrochemical deposition method. Reproduced with permission,[57] Springer Nature. (h) Schematic illustration of interstitial Mo atom doping on MoS_2 using a cold hydrogen-plasma method. Reproduced with permission,[59] American Chemical Society.

are crucial to improving the HER-activity of the basal plane.[13,70,84,85] Currently, a variety of vacancy-engineering strategies, such as Ar plasma treatment,[32] electron/ion beam/laser irradiation,[86] strain (physical etching),[87] solvothermal growth,[88] CVD annealing,[83] and electrochemical desulfurization (chemical etching)[89] have been developed. Those vacancies can be divided into transition metal vacancies and chalcogenide vacancies in TMDCs, as shown in Fig. 6a.

To investigate the influences of structures and concentrations of chalcogenide vacancies on the basal plane for HER;

Zhang and co-workers employed mild H_2 annealing to precisely create SVs in the monolayer MoS_2 at different temperatures and achieved isolated, paired, and clustered SVs (Fig. 6b). In another example, Tsai et al. used electrochemical desulfurization to introduce SV in the basal plane of the monolayer MoS_2 with a concentration of 21.9 at% (Fig. 6c). Combining the DFT calculations (Fig. 6d), the authors demonstrated that only isolated atomic vacancies can be considered localized states to maximize the charge hopping probability, and thus significantly increase the turnover frequency of Mo atoms (TOF_{Mo} =

19072 | J. Mater. Chem. A, 2022, 10, 19067–19089

This journal is © The Royal Society of Chemistry 2022

Fig. 5 Nonmetal-doping strategy of 2D-TMDCs for HER. (a) The calculated E_{CBM} and E_{VBM} of pristine and nonmetal-doped $MoSe_2$ monolayers. Reproduced with permission,[76] Springer Nature. (b) Atomic structure (left) and scanning tunneling microscopy (STM) images (right) of the exfoliated MoS_2 monolayer in the air after one month, and its corresponding HER performance (c). Reproduced with permission,[77] Springer Nature. Schematic illustration of carbon (C)-doped MoS_2 (d) and its corresponding HER performance in an alkaline electrolyte (e). Reproduced with permission,[79] Springer Nature. (f) Janus MoS_2 monolayer synthesized through a plasma-enhanced CVD method. Reproduced with permission,[81] Springer Nature. (g) Polarization curves of nitrogen (N)-doped MoS_2 samples. Reproduced with permission,[75] Wiley-VCH.

10 s^{-1}) of samples (Fig. 6e).[83,89] Nevertheless, they also observed that a further increase in the vacancy density would form clustered SVs, which could produce deep trapping levels to lower the electronic properties, consequently degrading HER performance. To improve the vacancy density, both Lei Li and Xin Wang *et al.* created much higher concentrations of SVs in MoS_2 compared to the above studies. They impressively found that the unsaturated Mo atoms acted as the active sites, which could introduce gap states favorable for hydrogen bonding, leading to an excellent per-site turnover frequency (1000 s^{-1} and 10 000 s^{-1} corresponding to the overpotentials of 200 mV and 300 mV in their work).[88,90]

On the other hand, compared with the above non-metal vacancies, Yang *et al.* showed that a large number of Mo vacancies were formed in CVD-grown MoS_2 after Helium ion irradiation, while they found a lower HER activity (Fig. 6f and g).[86] This phenomenon can be explained by the fact that the physical etching could severely damage the atomic structures of

TMDC's basal planes, such as holes, cracks, and curl zones and degrade their electronic properties. Note that these non-metal vacancies would play a more positive role in improving the HER performance, as compared to the metal ones.

3.3 GB strategy

Recent studies have demonstrated that GBs possess a high catalytic activity due to the synergistic effect raised from the local strain and unsaturated sites.[91] Different from the above doping and vacancies, GB is a type of 1D defect (besides edge), with dreidel-shaped dislocation cores and ringed motifs.[70,85] They can be divided into homo-phase and hetero-phase structures according to their neighboring phases, as shown in Fig. 7a. The main approaches to synthesizing GBs consist of CVD,[92,93] molecular beam epitaxy (MBE),[94] physical vapor deposition (PVD),[95,96] metal–organic chemical vapor deposition (MOCVD),[97,98] hydrothermal methods,[99] and plasma.[93] Additionally, other factors such as the fast kinetic processes, the multiplicity of phases and ingredients,

This journal is © The Royal Society of Chemistry 2022

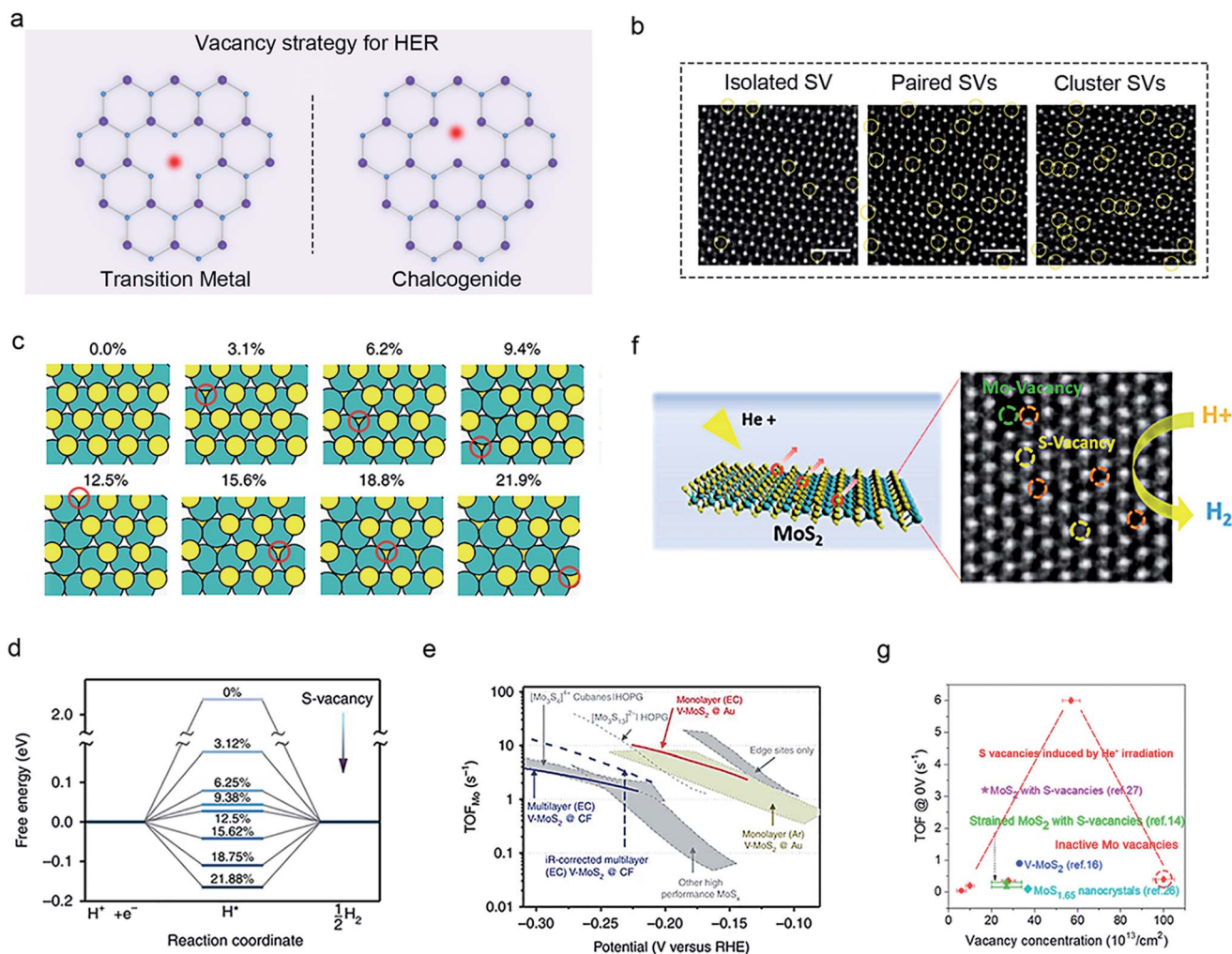*J. Mater. Chem. A*, 2022, **10**, 19067–19089 | **19073**

Fig. 6 Vacancy strategy of 2D-TMDCs for HER. (a) Schematic illustration of two kinds of vacancies in TMDCs: transition metal vacancy (left) and chalcogenide vacancy (right). (b) Scanning transmission electron microscopy (STEM) images of the isolated S, paired S, and clustered S vacancies in a MoS$_2$ monolayer generated by varied H$_2$-annealing conditions. Reproduced with permission,[83] Wiley-VCH. (c) Schematic illustration of the optimized structures of MoS$_2$ with varied S-vacancy concentrations. The free energy diagram of S-vacancy sites (d) and turnover frequencies per surface Mo atom (e) for the samples in (c). Reproduced with permission,[89] Springer Nature. Defective MoS$_2$ film fabricated through a helium-ion irradiation method (f) and its corresponding turnover frequency (TOF) at varied vacancy concentrations (g). Reproduced with permission,[86] American Chemical Society.

low symmetry, and crystalline substrate could also promote the formation of GBs.[33,94]

For example, Zhu *et al.* firstly calculated the Gibbs free energy of GBs in hetero/homo-phase MoS$_2$ (Fig. 7b). 2H–1T GBs possess extremely low H adsorption energy, which improves the basal plane's activity.[93] Furthermore, the authors also optimized the 2H–1T GB density of MoS$_2$ (hundred-nanometers-size domains) by using argon plasma treatments (Fig. 7c). It turned out a very low overpotential of ~136 mV *vs.* RHE, a Tafel slope of ~73 mV dec^{-1}, and long-term stability in acidic and alkaline conditions, as shown in Fig. 7d. Alternatively, Lee and co-workers reported the 1T′–2H hetero-phase GBs of MoTe$_2$ *via* CVD (Fig. 7e). They found a positive linear correlation between the exchange current density and the length of the MoTe$_2$ 2H–1T′ GBs, allowing for an excellent TOF value of 317 s^{-1} because of the charge accumulation and local band bending at the GBs (Fig. 7f).[92] To achieve an

ultra-high density of 2H–2H homo-phase GBs, in our previous work, we employed the Au-quantum-dots (QDs)-assisted vapor-phase growth in producing sub-10 nm-domain MoS$_2$ films with a GB density up to ~10^{12} cm^{-2} (Fig. 7g). It gave an excellent HER performance (onset potential: −25 mV *vs.* RHE and Tafel slope: 54 mV dec^{-1} in Fig. 7h).[33]

3.4 Phase strategy

Crystal phase-controlled synthesis of TMDCs is a promising strategy that could significantly affect catalytic activity and conductivity as well. Fig. 8a presents various polymorphs of TMDCs, including 2H, 3R, 1T, 1T′, and 1T$_d$ phases, depending on the interaction and coordination between the transition metal and chalcogen.[26,100–102] Basically, the triangular prism-coordinated TMDCs are typical semiconductors (2H or 3R phase) and have a lower conductivity than metallic octahedral-
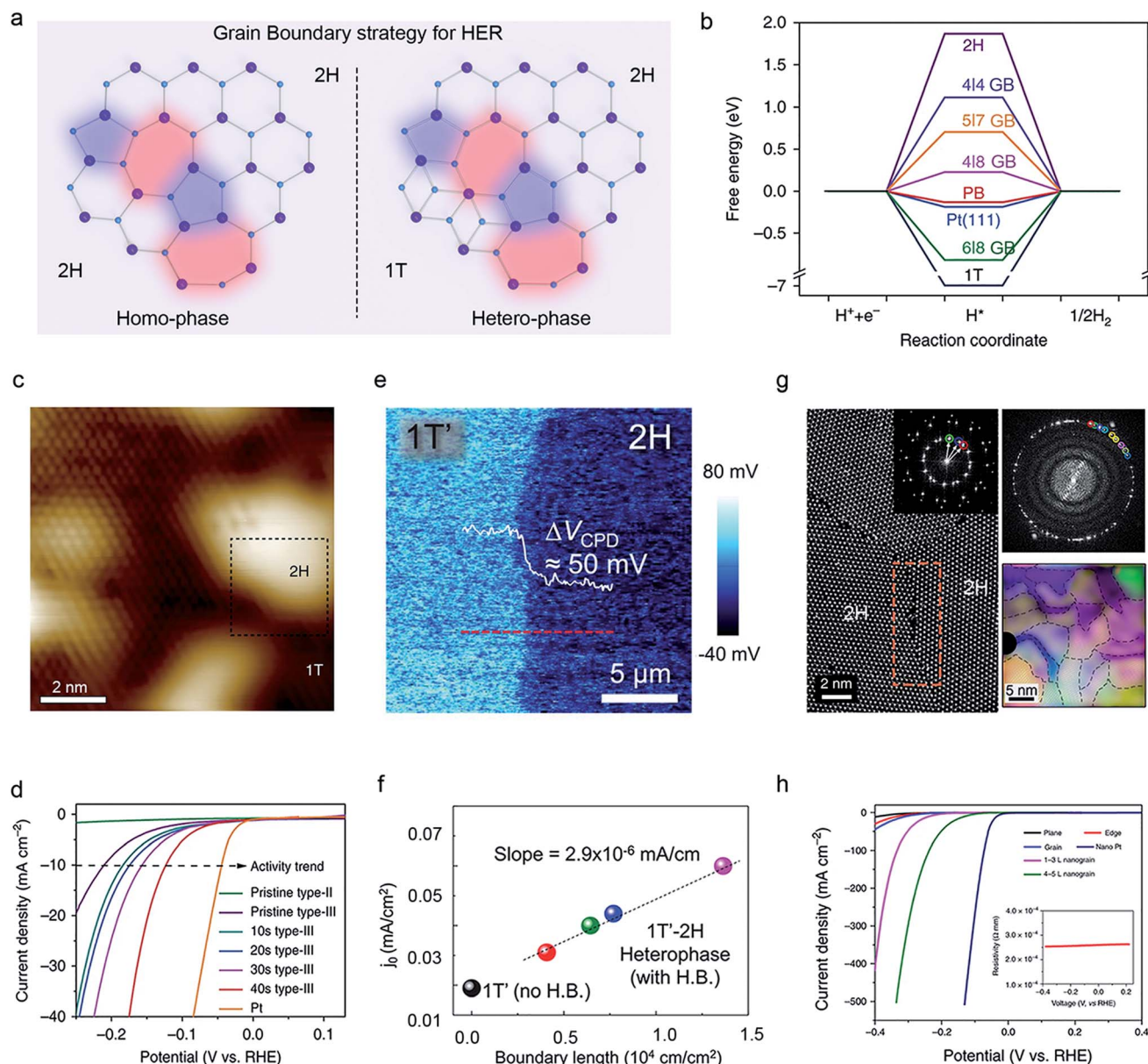
19074 | *J. Mater. Chem. A*, 2022, **10**, 19067–19089

This journal is © The Royal Society of Chemistry 2022

Fig. 7 Grain boundary (GB) strategy of 2D-TMDCs for HER. (a) Schematic illustration of the two kinds of GBs: homo-phase and hetero-phase. (b) Comparison of the ΔG_{H*} on 2H-MoS$_2$, 1T-MoS$_2$, Pt (111), and 2H–1T hetero-phase GB, and 2H–2H homo-phase GB. Reproduced with permission,[93] Springer Nature. STM image of the 2H–1T hetero-phase GB of MoS$_2$ (c) and the polarization curves with varied GB densities (d). Reproduced with permission,[93] Springer Nature. Charge potential mapping across a 1T′–2H hetero-phase GB of MoTe$_2$ (e) and its exchange-current-density as a function of the GB length (f). Reproduced with permission,[92] Wiley-VCH. Atomic structures of 2H–2H homo-phase GBs in the MoS$_2$ nanograin film (g) and their polarization curves (h) obtained from the microcells. Reproduced with permission,[33] Springer Nature.

coordinated ones.[103,104] In the past, various strategies have been used to synthesize metal-phase group VI TMDCs, such as alkali metal intercalation,[28,101,104–108] electron beam irradiation,[104,109] plasma bombardment,[110] pressure and strain,[111] high magnetic field hydrothermal reaction,[112] and electrostatic doping,.[113] Using the first-principles calculations, Fan and co-workers suggested that only the basal plane of 1T′-MoS$_2$ should be active in the HER, contrary to 2H-MoS$_2$ (Fig. 8b).[114] Unfortunately, it was found in the experiments that most 1T or 1T′-phase TMDCs are metastable and easily converted into their 2H counterparts.[26,106] To abbreviate this issue, Voiry et al. adopted

the Li-intercalation-based chemical-exfoliation method to produce stable 1T-MoS$_2$ nanosheets with a negatively-charged surface. Those nanosheets exhibited an excellent catalytic activity toward HER (Fig. 8c).[28] Subsequently, Liu and Yu et al. designed an alkali metal atom (K)-assisted CVD method for growing stable 1T′-TMDC monolayers (such as MoS$_2$, WS$_2$, WSe$_2$, MoSe$_2$), as shown in Fig. 8d.[104,105] They claimed that the intercalation of alkali metals could significantly reduce the formation energy of the metal phase TMDCs. A better HER performance was also observed in their samples compared to that of 2H phases, as shown in Fig. 8e. To more clearly elaborate

Fig. 8 Phase-engineering strategy of 2D-TMDCs for HER. (a) Schematic illustration of the different phase structures of TMDCs. Reproduced with permission,[26] Springer Nature. (b) The first and second H structures adsorbed on the surfaces of 1H, 1T, and 1T′ MoS$_2$, and the correspondingly calculated Gibbs free energy, respectively. Reproduced with permission,[114] Royal Society of Chemistry. (c) HER activity of solution-exfoliated 1T and 2H MoS$_2$ nanosheets. Reproduced with permission,[28] American Chemical Society. Phase-controlled CVD strategy of 1T′ MoS$_2$ monolayer (d) and its corresponding polarization curve (e). Reproduced with permission,[105] Springer Nature. The fabrication process of three types (EM-1, EM-2, and EM-3) of electrochemical microcells (f) and their corresponding HER performances. Inset: optical microscopy image of EM-1. Scale bar, 20 μm (g). Reproduced with permission,[29] Springer Nature.

on the activity of the 1T′ phase, Yu *et al.* employed both thermal annealing and laser irradiation to realize a smooth phase transformation from 1T′-MoS$_2$ to 2H-MoS$_2$, and verify the enhanced HER activity solely based on the 1T′ basal phase using three microcells (Fig. 8f and g).[104]

3.5 Superlattice strategy

With the help of topological physics engineering, superlattices can optimize the electronic structure and energy bands of TMDC catalysts.[115–117] There are two types of superlattices: traditional (periodic stacking of different layered materials) and

moiré ones (twisted structure of similar 2D bilayers), as shown in Fig. 9a. Most TMDC superlattices with different stacking orders and twists between layers have been obtained by layer-by-layer restacking,[118–120] CVD,[121] laser molecular beam epitaxy (LMBE),[122,123] electrochemical–molecular intercalation,[59,124] hydrothermal methods,[125,126] capillary-force-driven rolling-up,[127] etc.

In theory, Xiong et al. demonstrated the bilayer models of MoS_2/graphene, layered double hydroxide (LDH)/G, and MoS_2/LDH superlattices for HER. The enhanced electrocatalytic

activity was observed in MoS_2/LDH, attributed to significant electron accumulation at its interface that could modulate the intermediates' adsorption energies in HER pathways (Fig. 9b).[128] In the experiment, Guo et al. developed an n-type TaS_2–N_2H_4 hybrid superlattice through a spontaneous molecular-intercalation method at room temperature (Fig. 9c). It has high electrical conductivity and a low work function, confirmed by the Kelvin probe force microscope (KPFM), showing an excellent HER activity (Fig. 9d).[59] On the other hand, using an LMBE technique, Jiang et al. reported a bilayer MoS_2
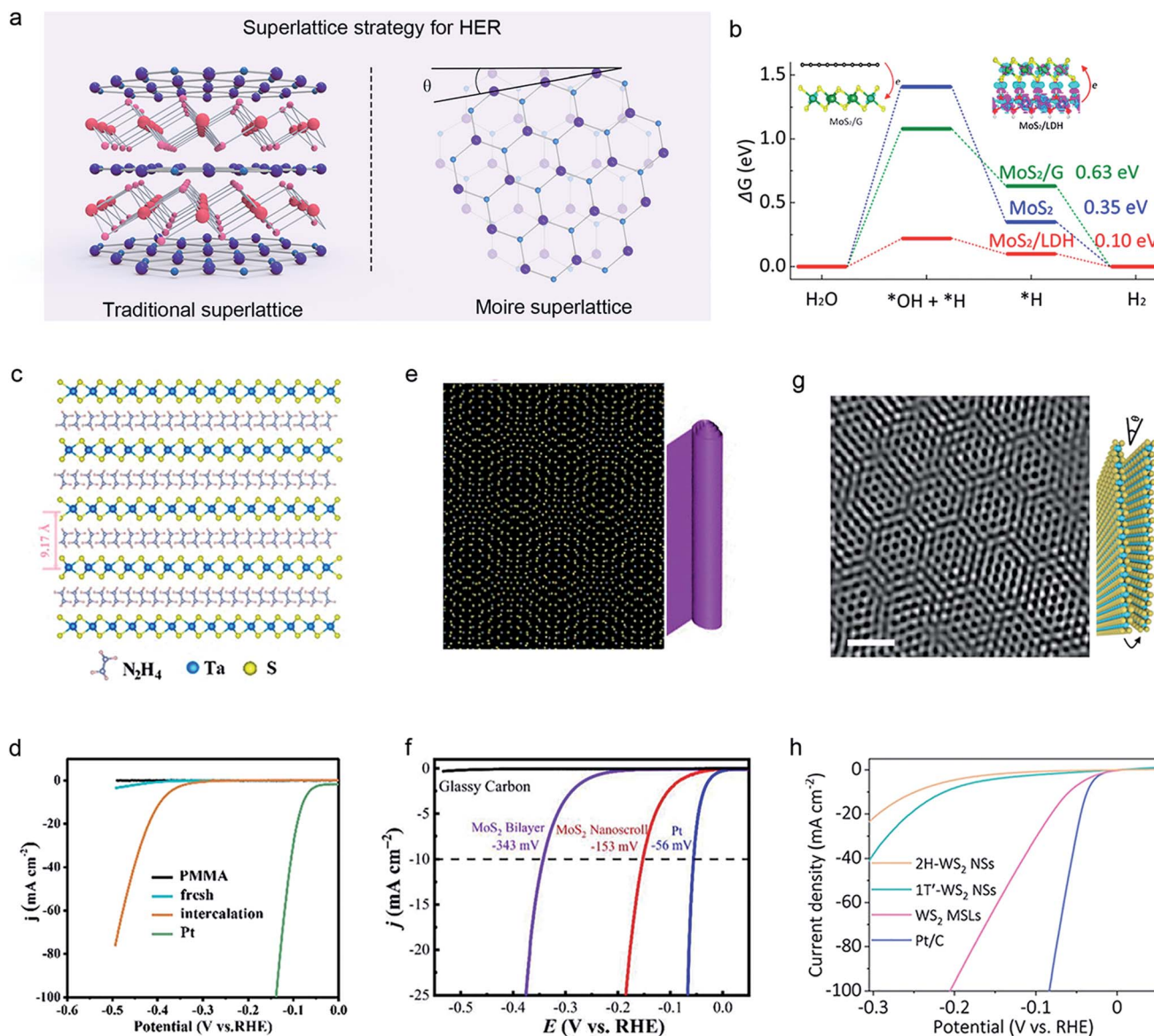

Fig. 9 Superlattice strategy of 2D-TMDCs for HER. (a) Schematic illustration of two kinds of superlattices: traditional superlattice (left) and moiré superlattice (right). (b) Comparison of the Gibbs free energies of the adsorbed H on MoS_2, MoS_2/graphene, and MoS_2/layered double hydroxide (LDH). Reproduced with permission,[128] American Chemical Society. The atomic structure of the TaS_2–N_2H_4 hybrid superlattice (c) and its corresponding HER performance (d). Reproduced with permission,[59] American Chemical Society. Structures of the moiré superlattice of a MoS_2 nanoscroll (e) and the corresponding polarization curves (iR-corrected) (f). Reproduced with permission,[123] American Chemical Society. High-resolution transmission electron microscopy (HRTEM) image of the WS_2 moiré superlattice formed by a layer-slipping method (g) and the corresponding iR-corrected polarization curves (h). Scale bar, 1 nm. Yellow and cyan balls represent S and W atoms, respectively. Reproduced with permission,[126] Springer Nature.

This journal is © The Royal Society of Chemistry 2022

J. Mater. Chem. A, 2022, 10, 19067–19089 | 19077

nanoscroll (twisted angle $\theta \approx 7.3°$) having a moiré superlattice structure (Fig. 9e). Such a structure could extremely reduce the interlayer potential barrier to improve the hopping efficiency of electron transfer, achieving a boosted electrocatalytic performance with η_{10} of −153 mV vs. RHE and Tafel slope of 73 mV dec^{-1}, as shown in Fig. 9f.[123] Additionally, Xie and co-workers found a nanoconical array WS$_2$ with moiré superlattices (Fig. 9g), showing an intriguing HER performance (the low overpotential η_{10} of 60 mV vs. RHE in the Fig. 9h).[126] The underlying mechanism is attributed to the fact that the twisted WS$_2$ bilayer has lower Gibbs free energy than the normal WS$_2$. The above approaches have enriched our current toolbox for designing superlattices and provide great potential for water-splitting applications.

4. External regulation

Besides the above internal methods, external control methods, such as the electric field, strain, substrates, and hetero-structures, have attracted considerable interest in activating the basal plane with a high degree of freedom.[36] For example, the applied electric field and strain can realize a smooth tunning of their catalytic activities. Conductive-carbon-based or metal-based substrates provide alternatives to improving the electron-injection efficiency for HER. Constructing HER-active materials (such as hydroxides, oxides, and carbides) onto TMDC basal planes to form the heterostructures presents another promising strategy.

4.1 Electric-field strategy

Applying a vertical electric field on TMDCs could enhance the HER efficiency by increasing the electrical conductivity, reducing the ΔG_{H*}, as well as adjusting the distribution of reactants.[104,129,130] It can serve as a high-degree-of-freedom strategy for tuning the basal plane activity of TMDCs smoothly.[36] In 2017, Mai et al. first explored the influence of the electric field on the MoS$_2$ nanosheet through a back-gate microcell (Fig. 10b).[131] They observed that in the absence of an electric field, a current density of 100 mA cm^{-2} required an overpotential of 240 mV. However, as the gate voltages increased up to 5 V, a significantly-reduced overpotential (down to 38 mV) was achieved, comparable to that of the Pt electrode, as shown in Fig. 10c. This improved HER efficiency could be attributed to lowering both MoS$_2$ itself resistance and the Au–MoS$_2$ contact barrier under a positive electric field. Later, a similar phenomenon was also observed in other works,[132–134] further confirming that the electric field can improve the electron injection process during the HER process.

Except for the improvement of the conductivity, the electric field can also regulate the ΔG_{H*} of the TMDCs basal planes or adjust the distribution of reactants in an electrolyte. For example, Frisbie et al. developed an electrochemical flow cell allowing the simultaneous measurements of electrical and electrochemical properties (Fig. 10d). However, they rarely observed a change in the sheet resistance of the monolayer MoS$_2$ when increasing the back-gate voltages (Fig. 10e).[135]

Alternatively, a significant drop in ΔG_{H*} was found because the Mo atoms next to the S vacancies on the basal plane accumulate excess electrons under the positive electric field, resulting in an enhanced HER performance.[136] Those results suggested that the electric field dominates ΔG_{H*} of the monolayer MoS$_2$ rather than its conductivity in HER. A similar phenomenon was also observed in bipolar semiconductors.[45] Fig. 10f shows H atoms adsorbed on a WSe$_2$ nanosheet, as obtained from the DFT calculations. The positive electric field provided more electron carriers for the bipolar WS$_2$, reducing the free energy (Fig. 10g).

The electric field can also adjust the distribution of charged reactants at the catalyst–electrolyte interface during the HER process.[137] Mai et al. used metallic VSe$_2$ as the working electrode and found that H$_3$O$^+$ prefers to accumulate at the interface (Fig. 10h and i).[110] Therefore, they claimed that the Volmer step in the HER process was accelerated, thus increasing the overall reaction rate. It is worth emphasizing that the electric field regulation is a complex strategy. One or more factors, such as the contact barrier of the whole system, the concentration of reactants, the conductivity of catalysts, and the transfer process of charges, would affect the reaction.

4.2 Strain strategy

Due to their atomic thickness, TMDC nanosheets are very sensitive to strain,[138–140] while impressively, they can withstand up to 23 GPa (11%) mechanical strain.[141] According to the d-band model,[142–144] the strength of H adsorption on the catalyst is crucial to the d-band position, and a tensile strain can upshift it to reduce occupied states of antibonding orbitals, promoting the H-atom adsorption.[145,146] This electronic theory could also be suitable for strained TMDCs,[146] and the strain would play a vital role in the H adsorption during the HER process. Here, we discuss three strain strategies: lattice mismatch, bending substrates, and textured strain.

A lattice mismatch can induce a local strain on TMDC materials.[147–149] For example, Chhowalla et al. prepared highly distorted 1T–WS$_2$ nanosheets using an intercalation-based chemical exfoliation method.[42] The STEM image shows a lattice mismatch in WS$_2$ nanosheets (Fig. 11c), and the inset confirmed that this mismatch could cause a large area of local strain (about 3%) on the basal plane. As a result, the free energy could be tuned to be close to 0 when the strain value was 2.7%, showing an excellent performance of the highly distorted 1T–WS$_2$ nanosheets (Fig. 11d).

Being different from the above lattice mismatch, constructing bending strain and texture strain usually requires templates such as 3D nanoporous gold (NPG),[150,151] nanofibers,[152] polymer substrate,[153] and nanocones.[32,154] For example, Tan et al. constructed single-Ru-atom-anchored nanoporous MoS$_2$ (denoted as Ru/np-MoS$_2$) by NPG (Fig. 11e).[151] It was found that the curved structure could introduce strain around the Ru-atom in the basal plane, the strength of which was tailored simply by the sample's ligament size. A larger strain in the Ru/np-MoS2 catalyst results in better performance, and a η_{10} of 30 mV, as well as a Tafel slope of 31 mV dec^{-1}, was finally achieved, as shown in Fig. 11f. Operando X-ray absorption spectroscopy (XAS) revealed that the

19078 | J. Mater. Chem. A, 2022, **10**, 19067–19089

This journal is © The Royal Society of Chemistry 2022

Fig. 10 Electric field strategy of 2D-TMDCs for HER. (a) Schematic illustration of the electric field strategy for HER. (b) Schematic illustration of a three-electrode microcell based on a MoS$_2$ nanosheet for HER measurement. (c) Polarization curves at varied back-gate voltages, as obtained from the micro-cell in (b). Reproduced with permission,[131] Wiley-VCH. (d) The structure of a back-gated microcell. Inset: the optical images of a MoS$_2$-monolayer electrode. (e) The normalized sheet resistance of the MoS$_2$ electrode as a function of the electrode potential (V_W) at varied back-gate voltages (V_{BG}). Reproduced with permission,[135] American Chemical Society. (f) DFT calculation of an H-atom adsorbed on a WSe$_2$ nanosheet charged by the back-gate voltage (blue, purple, and green balls represent Se, W, and H atoms, respectively). (g) The Gibbs free-energy diagram of WSe$_2$ under different carrier concentrations. Reproduced with permission,[45] Wiley-VCH. (h) COMSOL simulation of the net charge distribution on the surface of a VSe$_2$ electrode at varied back-gate voltages. (i) Simulation results of charge concentrations on the surface (lines and dots represent H$^+$ and SO$_4{}^{2-}$, respectively). Inset: the net charge as a function of back-gate voltage. Reproduced with permission,[110] American Chemical Society.

strain could accelerate the mass transfer from the S-vacancy sites to Ru sites, amplifying the synergetic interaction between them. In another example, Li *et al.* created a wide range of texture strains on the basal plane of MoS$_2$ using a nanocone array method (Fig. 11g).[32] After comparing MoS$_2$, strain-only MoS$_2$ (S-MoS$_2$), and vacancy-only MoS$_2$ (V-MoS$_2$), strained-vacancy MoS$_2$ (SV-MoS$_2$) gave the best HER performance with a η_{10} of 170 mV, as shown in Fig. 11h (green areas referred to the contribution of strain to reactivity). They claimed that the tensile strain could narrow the MoS$_2$ bandwidth and shift the free energy toward thermoneutrality, thus enhancing the HER activity. It is worth mentioning that the strain, in combination with other methods,

e.g., vacancies,[87] can provide a more flexible way to regulate the catalytic performance of the basal planes.

4.3 Substrate strategy

The underlying substrates have been confirmed to facilitate the electron injection and modify the chemical property of catalysts to improve catalytic performance, *that is*, the substrate effect.[27,157,158] The conductive substrates can be classified into carbon materials and pure metals. The former mainly includes carbon black,[159] graphenes,[155,160,161] carbon nanotubes,[162,163] and carbon fiber.[156] The latter are Au, Ti, Ni,

This journal is © The Royal Society of Chemistry 2022

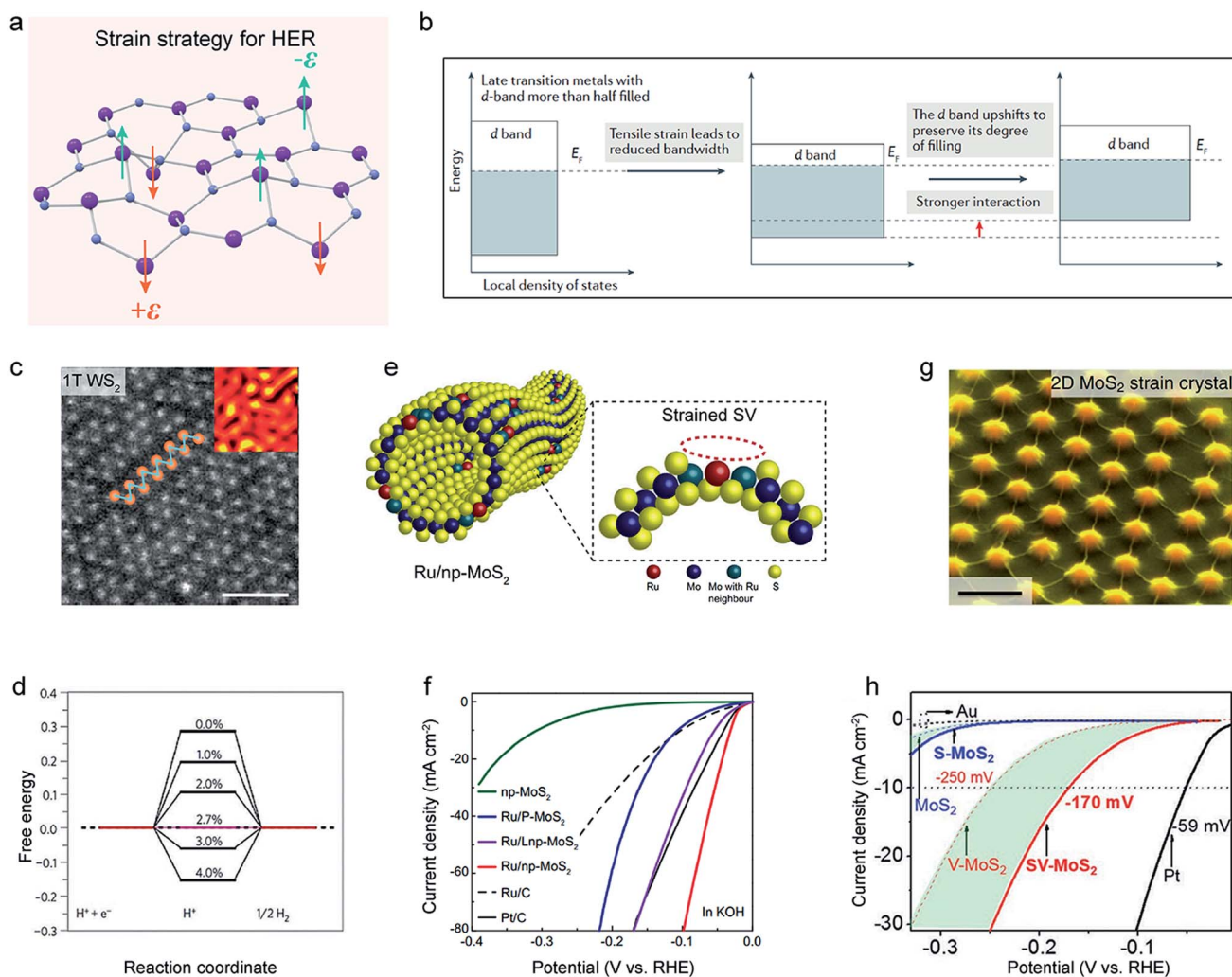*J. Mater. Chem. A*, 2022, **10**, 19067–19089 | **19079**

Fig. 11 Strain strategy of 2D-TMDCs for HER. (a) Schematic illustration of the strain strategy for HER. (b) The energy diagrams of the influence of tensile strain on the d-band position in late transition metals. Reproduced with permission,[145] Springer Nature. (c) High-resolution scanning transmission electron microscopy (STEM) images of the as-exfoliated WS_2. Inset: the strain tensor mapping obtained from the STEM images (black and yellow colors correspond to compressed and tensile regions). Scale bar, 1 nm. (d) The Gibbs free energy of $1T−WS_2$ varied by the tensile strain. Reproduced with permission,[42] Springer Nature. (e) Schematic illustration of the Ru/nanoporous MoS_2 (Ru/np-MoS_2). SV indicates sulfur vacancies. (f) Polarization curves of Ru/np-MoS_2, in comparison to those of nanoporous MoS_2 (np-MoS_2), Ru/plane MoS_2 (Ru/P-MoS_2), and Ru/larger ligament nanoporous MoS_2 (Ru/Lnp-MoS_2). Reproduced with permission,[151] Springer Nature. (g) False-color SEM image of a 2D strained MoS_2 monolayer on a nanocone array. Scale bar, 1 μm. Reproduced with permission,[154] Springer Nature. (h) Polarization curves of strained-vacancy MoS_2 (SV-MoS_2), in comparison to those of the Au substrate, pristine MoS_2, strained MoS_2 (S-MoS_2), and MoS_2 with vacancies (V-MoS_2). Reproduced with permission,[32] Springer Nature.

Pt, and so on.[40] The typical substrate is graphene. Shin *et al.* fabricated WS_2/reduced graphene oxide (WS_2/rGO) hybrid nanosheets using conductive rGO as the substrate (Fig. 12b).[155] Since the rGO substrate facilitates a rapid electron transfer to the WS_2 catalyst, WS_2/rGO nanosheets enhance HER performance compared with WS_2 alone, as shown in Fig. 12c. Extending to metal substrates, Liu *et al.* systematically investigated the catalytic performance of TaS_2 on the glass carbon plate, carbon fiber, Mo foil, and Au foil.[156] Among those substrates, the authors found that Au/TaS_2 has the best catalytic performance (33 mV dec^{-1} of Tafel plot in Fig. 12d) with the lowest ΔG_{H*} (Fig. 12e), which results from the ideal lattice mismatch at the TaS_2–Au interface (Fig. 12f).

On the other hand, substrates could also induce carrier doping to modify the activity of TMDC catalysts.[164,165] For instance, Cao *et al.* observed substrate-induced *n*-doping of the monolayer MoS_2 through the redshift of Raman spectra (Fig. 12g).[40] The DFT shows that such doping would improve the activity of the vacancies to activate the MoS_2 basal plane (Fig. 12h), and a higher doping level (Pt > Ni > Ti > Au) leads to lower adsorption energy of the sample, agreeing with the experiment results (Fig. 12i).

4.4 Heterostructure strategy

Heterostructures that were rationally designed by combining the advantages of each TMDC component together would
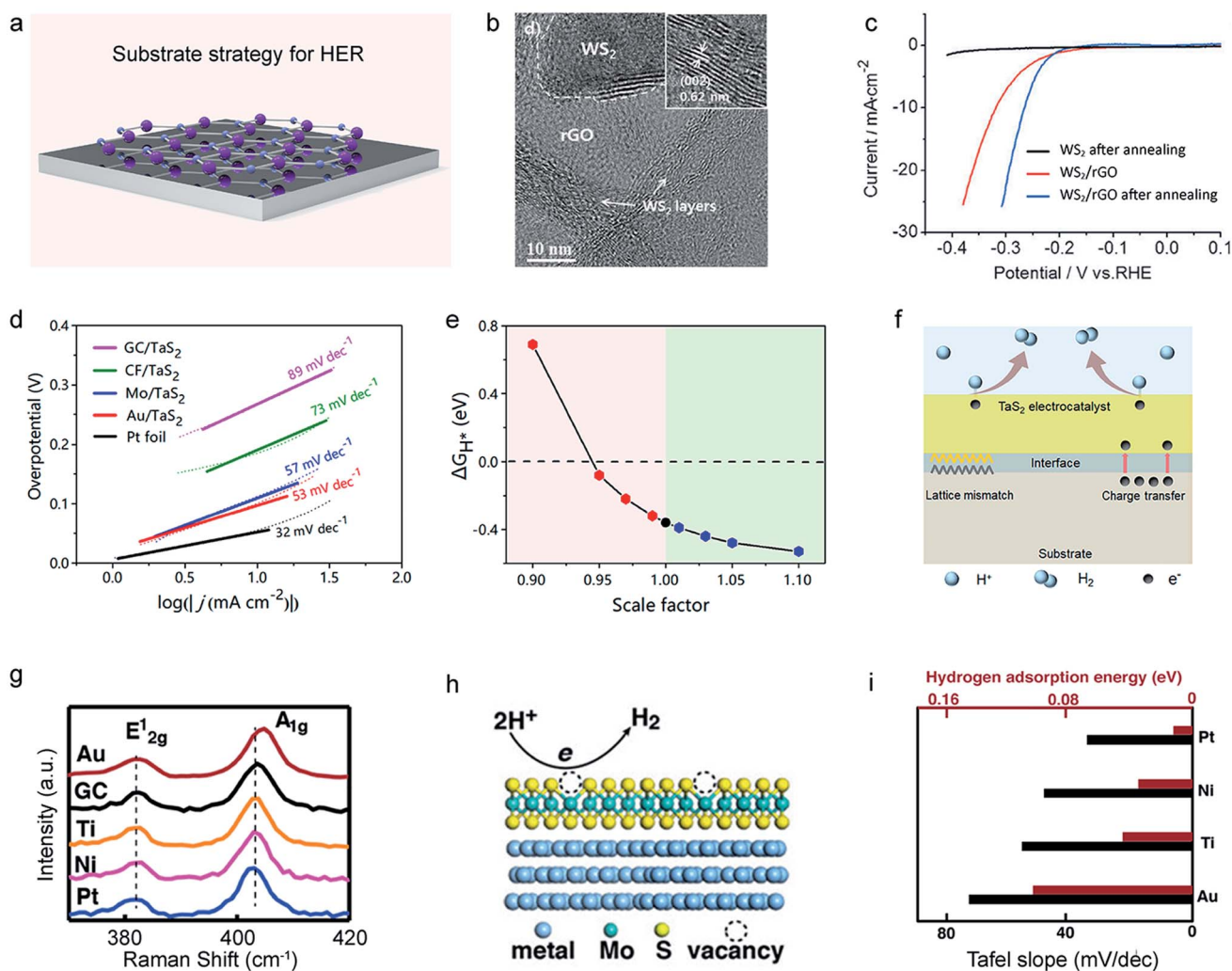
Fig. 12 Substrate strategy of 2D-TMDCs for HER. (a) Schematic illustration of the substrate strategy for HER. (b) HRTEM image of the WS_2/reduced graphene oxide (WS_2/rGO) hybrid nanosheet. Inset: the zoom-in image of the WS_2 nanosheet. (c) Polarization curves of the annealed WS_2/rGO hybrid nanosheets, in comparison to those of annealed WS_2 nanosheets and WS_2/rGO hybrid nanosheets. Reproduced with permission,[155] Wiley-VCH. (d) Tafel plots of TaS_2 samples on glass carbon (GC), carbon fibers (CF), Mo, and Au substrates. (e) The ΔG_{H*} of the TaS_2 nanosheet under the lattice-mismatch condition. (f) Schematic illustration of the substrate effect on a TaS_2 electrocatalyst. Reproduced with permission,[156] American Chemical Society. (g) Raman spectra of monolayer MoS_2 on Au, GC, Ti, Ni, and Pt substrates, showing the redshift of Pt > Ni > Ti > Au. (h) Schematic illustration of the substrate effect on a MoS_2 monolayer. (i) Calculated hydrogen adsorption energies and the measured Tafel slopes of a MoS_2 monolayer on Pt, Ni, Ti, and Au substrates. Reproduced with permission,[40] American Chemical Society.

possess a higher catalytic performance than those single components.[14,166,167] Here, we would discuss the synergistic effect[168,169] and the interfacial charge transfer[170–172] originating from heterostructures. So far, the synergistic effects have also been frequently observed in hydroxide/TMDC,[173–176] TMDC/TMDC,[177–180] oxide/TMDC,[181–183] and others.[184–187] As discussed in Section 2, the high adsorption energy of H_2O hinders the generation of H_{ad} intermediates, leading to sluggish kinetics in alkaline solution. To optimize HER pathways, Jiang et al. prepared a $Ni(OH)_2$/MoS_2 heterostructure, in which $Ni(OH)_2$ could serve as the dissociation promoter, thereafter, H_2 was generated on the MoS_2 basal plane.[188] DFT calculations also confirmed this synergistic effect, which could lower the H_2O adsorption energy from 0.75 eV to 0.05 eV, significantly

accelerating the reaction kinetics. A Tafel plot of 60 mV dec^{-1} was finally obtained in this heterostructure, much better than that of the pristine basal plane (96 mV dec^{-1}), as shown in Fig. 13d.

It was found that heterostructures could also optimize the electronic structure and the mass/electron transfer. For example, Cha et al. synthesized MoS_2/WTe_2 vertical heterostructure with semi-metallic WTe_2 as the bottom layer.[189] They claimed that a low Schottky barrier in the heterostructure tends to rapidly inject electrons from the bottom WTe_2 to the top MoS_2. Consequently, the catalytic activity of MoS_2 in the heterostructure is better than that of the WTe_2 edge-contacted one. That is, the former had a larger contact area than the latter (Fig. 13g), thus showing a shorter pathway of charge

This journal is © The Royal Society of Chemistry 2022

J. Mater. Chem. A, 2022, **10**, 19067–19089 | **19081**

Fig. 13 Heterostructure strategy of 2D-TMDCs for HER. (a) Schematic illustration of the heterostructure strategy for HER. (b) Schematic illustration of the water activation process for the Ni(OH)$_2$/MoS$_2$ heterostructure in an alkaline solution. H, O, Mo, S, and Ni atoms are shown in white, red, cyan, yellow, and blue, respectively. The free energy diagram (c) and the Tafel plots (d) for MoS$_2$, Ni(OH)$_2$, and Ni(OH)$_2$/MoS$_2$. Reproduced with permission,[188] Elsevier. (e) The aligned band structure of the MoS$_2$/WTe$_2$ heterostructure. (f) The corresponding polarization curves of the MoS$_2$/WTe$_2$ heterostructure. (g) Comparison of the HER mechanisms of the MoS$_2$/WTe$_2$ heterostructure (bottom) and MoS$_2$ with WTe$_2$ edge-contact (top). Reproduced with permission,[189] Wiley-VCH. HRTEM image (h) and the TOF(i) of the in-plane 1T-2H MoS$_2$ hetero-structure. Reproduced with permission,[125] Wiley-VCH.

during the HER process. In another example, Yang *et al.* reported a stable in-plane 1T-2H MoS$_2$ heterostructure using an annealing treatment method (Fig. 13h).[125] They demonstrated a huge improvement in HER properties in the alkaline solution (TOF: 13.14 and 1.61 H$_2$ s^{-1} at 250 mV for heterostructure and 2H-MoS$_2$ nanosheet, respectively), as shown in Fig. 13i. This enhancement was attributed to the rapid electron transport and abundant active sites, both of which facilitate activating the inert basal plane of 2H-MoS$_2$. It can be seen that those above heterostructures can combine the advantages of each component, significantly activating the basal plane of TMDCs. What is more, the recent emergence of machine learning could assist in screening the types and structures,[190] which will be helpful in the design of high-performance heterostructure catalysts.

5. Summary and outlook

Electrocatalytic hydrogen production, basically, is an interfacial reaction, where the adsorption and desorption behavior of hydrogen atoms, that is, ΔG_{H*} as an important parameter, dominate the reaction rate. Benefiting from their stable and atom-thin (<1 nm) nature, 2D TMDCs themselves act as an interface and possess the potential of exposing nearly all of their atoms to the electrolyte. This unique character makes 2D TMDC ideal candidates for HER catalysts and the corresponding mechanism study. Unfortunately, in respect of most non-metallic TMDCs, their basal plane is usually inert. In the past ten years, substantial studies have thus been undertaken to activate the basal plane through strategies based on internal regulation such as doping, vacancies, phases, GBs, super-lattices, or external regulation, such as the electric field, strain, substrates, and heterostructures. We summarized the

19082 | *J. Mater. Chem. A*, 2022, **10**, 19067–19089

This journal is © The Royal Society of Chemistry 2022

characteristics of all strategies mentioned above in Table 1 and enumerated their corresponding principles, active types, and representative examples. Among them, some strategies activate the basal plane by creating dispersed active sites, such as doping, vacancies, and GBs. In contrast, the others did it by modulating the whole plane's activity lane, such as phases, superlattices, the electric field, and heterostructures.

Although significant progress has been made to improve the HER activity of TMDC's basal planes, some challenges remain in the above strategies. For example, with respect to the dispersed active sites, the activating effectiveness depends largely on their intrinsic activity and density, however, a high density of the sites (for example, vacancies) will destroy the 2D layered structure. Therefore, we need to strike a balance between the activity and stability for those activating strategies since both will affect the key figure of merit of HER performances. On the other hand, adopting phase-transition, superlattices, and heterostructures enable a whole active layer of 2D TMDCs, while their structural stability and reproducibility are still challenges. For example, octahedrally-coordinated 1T-phase and intercalated hybrid superlattices have low thermodynamic stability. Alternatively, the electric field and heterostructures also lead to a whole active layer, however, their mechanisms are still challenging to clarify, such as the inter-layer coupling in heterostructures, and the apparent differences among the electron injection, and electron transport, as well as ion-redistribution under the applied electric field.

Despite the above challenges, there are also many intriguing directions for efficiently activating TMDC's basal planes. Here, we provide personal perspectives on opportunities to be explored in this emerging field.

The first is a joint strategy. Such strategies have their own advantages or disadvantages, as discussed above. They would rouse a joint strategy that can combine two or three strategies to make full use of all their advantages (that is, one plus one is greater than two). A typical example is strained-S vacancies in the MoS$_2$ basal plane.[32] For only SVs, increasing their concentrations would continually lower ΔG_{H*}, while its high level (>19%) would lead to poor stability. On the other hand, it is insufficient to activate the basal plane only by the strain strategy, even at a high strain. Interestingly, taking them together would only require ∼11% of SVs to realize an optimal

Table 1 Summary of the strategies for activating the TMDC basal planes

Strategy	Principle	Active types	Examples	Material/ structure	η_{10} (mV)	Tafel slope (mV dec^{-1})	Electrolyte	Ref.
Doping	Engineer locally uncoordinated active sites	Dispersed sites	Metal-doping	Pd–MoS$_2$	89	62	0.5 M H$_2$SO$_4$	62
			Nonmetal-doping	Carbon–MoS$_2$	45	46	1 M KOH	79
Vacancies	Engineer locally unsaturated site	Dispersed sites	Isolated-S vacancies	30 He$^+$–MoS$_2$	200	90	0.5 M H$_2$SO$_4$	86
			Cluster-S vacancies	Repaired 2H-MoS$_2$	300	85	0.5 M H$_2$SO$_4$	88
Phases	Increase the conductivity and lower the hydrogen absorption energy	Whole plane	1T′ phase	1T′-MoS$_2$	65	100	0.5 M H$_2$SO$_4$	29
			1T phase	1T-MoS$_2$	230	45	0.5 M H$_2$SO$_4$	108
GBs	Engineer unsaturated-site 1D channel	Dispersed 1D sites	2H–2H GBs	MoS$_2$ nanograin film	25	50	0.5 M H$_2$SO$_4$	33
			2H–1T GBs	2H–1T-MoS$_2$ GB	260	85	0.5 M H$_2$SO$_4$	93
Superlattices	Improve the activity by interfacial electronic coupling	Whole plane	Moiré superlattice	WS$_2$ moiré superlattice	60	42	0.5 M H$_2$SO$_4$	126
			Layer-stacked superlattice	TaS$_2$/N$_2$H$_4$ superlattice	0.4	76	0.5 M H$_2$SO$_4$	191
Electric field	Facilitate electron injection and ion-redistribution	Whole plane	Vertical electric field	Monolayer MoS$_2$	176	100	0.5 M H$_2$SO$_4$	135
Strain	Lower the hydrogen absorption energy	Dispersed sites	Lattice-mismatch induced stain	Distorted 1T WS$_2$	235	60	0.5 M H$_2$SO$_4$	42
			Bending stain	Ru/nanoporous MoS$_2$	30	31	1 M KOH	151
			Textured strain	Strained-vacancy MoS$_2$	131	48	0.5 M H$_2$SO$_4$	32
Substrates	Enhance electron injection, and activity by doping	Whole plane	Metal-based substrates	TaS$_2$ on Au	101	53	0.5 M H$_2$SO$_4$	156
			Carbon-based substrates	WS$_2$ on rGO	264	58	0.5 M H$_2$SO$_4$	155
Heterostructures	Synergistic effect	Whole plane	Hydroxide/TMD heterostructure	Ni(OH)$_2$/MoS$_2$	80	60	1 M KOH	188
	Accelerate interfacial charge transfer	Whole plane	TMD/TMD heterostructure	MoS$_2$/WTe$_2$	135	40	0.5 M H$_2$SO$_4$	189

condition of $\Delta G_{H*} = 0$ eV, which helps preserve the stability of the layered structures.

Second, phase-engineering TMDC strategy. As an important parameter of layered TMDs, the crystal phase is usually decisive to their properties. For example, most 2H TMDCs, *e.g.*, 2H-MoS$_2$, MoSe$_2$, WS$_2$, WSe$_2$, *etc.*, are very stable in air/water and can withstand the acidic/basic electrolyte as well as high temperatures (>400 °C in hydrogen atmosphere), while the only drawback they meet is the inertness of the basal plane for HER. On the contrary, their metallic counterparts, such as 1T-MoS$_2$, and 1T'-MoS$_2$, the whole basal planes are HER-active. However, their large-scale or pure-phase syntheses remain challenging to date due to their metastable nature. Therefore, under a trade-off of structural stability and HER activity, phase-engineering TMDC materials, such as 2H–1T phase transform or direct 1T phase-controlled synthesis, would present a promising strategy to activate the basal plane in a sampling manner.

The third is electrical–electrocatalytic coupling. From a charge-flowing point of view, a typical electrocatalytic process usually involves three steps, including the first charge injection step from the conductive substrate to the catalyst, the later charge transport step inner the catalyst body, and finally, the charge transfer at the sites at the solid–liquid interface. It can be seen that, besides the activity sites, both the charge injection and transport steps are the key factors affecting the reaction happens. For example, Voiry *et al.* improved the electron injection (the first step) from the Au electrode to the 2H-MoS$_2$ catalyst using phase-engineered low-resistance contacts and achieved comparable performance to metallic edges and the 1T phase.[30] In another example, He *et al.* observed a self-gating effect at the TMDC nanosheet–electrolyte interface,[192] demonstrating that the electrocatalytic reaction itself can strongly modulate the conductance (the second step) of TMDC. Moreover, their semiconducting types (n, p, or bipolar) could strongly correlate with their electrocatalytic reactions (HER, OER, or both). Those typical works indicate the potential importance of electrical–electrocatalytic coupling in the HER process, which needs to be considered when exploring new activating strategies.

Last, but not least, is the potential of "single-atom-layer" catalysis. In our previous work, we reported a single-atom-layer Pt catalyst,[193] fabricated by a low-temperature amorphizing strategy of 2D PtSe$_2$ at a single-layer limit. This catalyst shows a fully-activated surface accessible to the HER, achieving high Pt-atom-utilization efficiency of up to ~26 wt% and a nearly 100% current density relative to a pure Pt surface. As a comparison, the single-atom catalyst that has dispersed atomic sites is capable of nearly 100% of the utilization efficiency while suffering from the limitations of low mass-loadings (*e.g.*, usually 5 wt% for Pt-based ones). Their differences can also be found in theory calculations, where the former employed H-coverage to evaluate the activity of the entire surface, while the latter only considered the H binding energy at single active sites. Based on the above discussions, it is also a desirable strategy to explore "single-atom-layer" catalysis based on 2D TMDCs because nearly all the atoms at the monolayer are accessible to catalytic reactions and are stable thermodynamically.

In summary, the activation of the TMDC basal planes can bring significant benefits to the HER. With the continuous enrichment of strategies, we anticipate that TMDCs can play a more vital role in electrochemical water splitting.

Author contributions

Y. H. conceived and initiated the project. H. X. and Z. S. carried out the literature survey, organized all the reference data, and prepared the figures. C. G. helped discuss the HER mechanism. All authors wrote the manuscript.

Conflicts of interest

There are no conflicts of interest to declare.

Acknowledgements

References

1 R. Dittmeyer, M. Klumpp, P. Kant and G. Ozin, *Nat. Commun.*, 2019, **10**, 1818.

2 F. Ueckerdt, C. Bauer, A. Dirnaichner, J. Everall, R. Sacchi and G. Luderer, *Nat. Clim. Change*, 2021, **11**, 384–393.

3 H. B. Wu, B. Y. Xia, L. Yu, X.-Y. Yu and X. W. Lou, *Nat. Commun.*, 2015, **6**, 6512.

4 M. Yu, K. Wang and H. Vredenburg, *Int. J. Hydrogen Energy*, 2021, **46**, 21261–21273.

5 Z.-J. Chen, G.-X. Cao, L.-Y. Gan, H. Dai, N. Xu, M.-J. Zang, H.-B. Dai, H. Wu and P. Wang, *ACS Catal.*, 2018, **8**, 8866–8872.

6 M. A. Abbas and J. H. Bang, *Chem. Mater.*, 2015, **27**, 7218–7235.

7 D. M. F. Santos, C. A. C. Sequeira, D. Macciò, A. Saccone and J. L. Figueiredo, *Int. J. Hydrogen Energy*, 2013, **38**, 3137–3145.

8 P. Wang, K. Jiang, G. Wang, J. Yao and X. Huang, *Angew. Chem., Int. Ed.*, 2016, **55**, 12859–12863.

9 A. Chalgin, C. Song, P. Tao, W. Shang, T. Deng and J. Wu, *Prog. Nat. Sci.: Mater. Int.*, 2020, **30**, 289–297.

10 D. Liu, L. Dai, X. Lin, J.-F. Chen, J. Zhang, X. Feng, K. Müllen, X. Zhu and S. Dai, *Adv. Mater.*, 2019, **31**, 1804863.

11 S. Dou, X. Wang and S. Wang, *Small Methods*, 2019, **3**, 1800211.

12 T. Rao, H. Wang, Y.-J. Zeng, Z. Guo, H. Zhang and W. Liao, *Adv. Sci.*, 2021, **8**, 2002284.

13 C. Tan, X. Cao, X. J. Wu, Q. He, J. Yang, X. Zhang, J. Chen, W. Zhao, S. Han, G. H. Nam, M. Sindoro and H. Zhang, *Chem. Rev.*, 2017, **117**, 6225–6331.

14 P. Prabhu, V. Jose and J.-M. Lee, *Matter*, 2020, **2**, 526–553.

15 Q. Lu, Y. Yu, Q. Ma, B. Chen and H. Zhang, *Adv. Mater.*, 2016, **28**, 1917–1933.

16 L. Guardia, J. I. Paredes, J. M. Munuera, S. Villar-Rodil, M. Ayán-Varela, A. Martínez-Alonso and J. M. D. Tascón, *ACS Appl. Mater. Interfaces*, 2014, **6**, 21702–21710.

17 M. Zhuang, L.-Y. Gan, M. Zou, Y. Dou, X. Ou, Z. Liu, Y. Ding, I. H. Abidi, A. Tyagi, M. Jalali, J. You, A. Cao and Z. Luo, *J. Mater. Chem. A*, 2018, **6**, 2900–2907.

18 S. Manzeli, D. Ovchinnikov, D. Pasquier, O. V. Yazyev and A. Kis, *Nat. Rev. Mater.*, 2017, **2**, 17033.

19 F. Jaramillo Thomas, P. Jørgensen Kristina, J. Bonde, H. Nielsen Jane, S. Horch and I. Chorkendorff, *Science*, 2007, **317**, 100–102.

20 C. Tsai, K. Chan, J. K. Nørskov and F. Abild-Pedersen, *Surf. Sci.*, 2015, **640**, 133–140.

21 H. Duan, C. Wang, G. Li, H. Tan, W. Hu, L. Cai, W. Liu, N. Li, Q. Ji, Y. Wang, Y. Lu, W. Yan, F. Hu, W. Zhang, Z. Sun, Z. Qi, L. Song and S. Wei, *Angew. Chem., Int. Ed.*, 2021, **60**, 7251–7258.

22 J. Zhang, J. Wu, H. Guo, W. Chen, J. Yuan, U. Martinez, G. Gupta, A. Mohite, P. M. Ajayan and J. Lou, *Adv. Mater.*, 2017, **29**, 1701955.

23 L.-J. Ma and H. Shen, *Appl. Surf. Sci.*, 2021, **545**, 149013.

24 M. Zhuang, G.-L. Xu, L.-Y. Gan, Y. Dou, C.-J. Sun, X. Ou, Y. Xie, Z. Liu, Y. Cai, Y. Ding, I. H. Abidi, A. Tyagi, K. Amine and Z. Luo, *Nano Energy*, 2019, **58**, 660–668.

25 C. Zhu, D. Gao, J. Ding, D. Chao and J. Wang, *Chem. Soc. Rev.*, 2018, **47**, 4332–4356.

26 Y. Chen, Z. Lai, X. Zhang, Z. Fan, Q. He, C. Tan and H. Zhang, *Nat. Rev. Chem.*, 2020, **4**, 243–256.

27 L. Lei, D. Huang, G. Zeng, M. Cheng, D. Jiang, C. Zhou, S. Chen and W. Wang, *Coord. Chem. Rev.*, 2019, **399**, 213020.

28 D. Voiry, M. Salehi, R. Silva, T. Fujita, M. Chen, T. Asefa, V. B. Shenoy, G. Eda and M. Chhowalla, *Nano Lett.*, 2013, **13**, 6222–6227.

29 Y. Yu, G.-H. Nam, Q. He, X.-J. Wu, K. Zhang, Z. Yang, J. Chen, Q. Ma, M. Zhao, Z. Liu, F.-R. Ran, X. Wang, H. Li, X. Huang, B. Li, Q. Xiong, Q. Zhang, Z. Liu, L. Gu, Y. Du, W. Huang and H. Zhang, *Nat. Chem.*, 2018, **10**, 638–643.

30 D. Voiry, R. Fullon, J. Yang, C. de Carvalho Castro e Silva, R. Kappera, I. Bozkurt, D. Kaplan, M. J. Lagos, P. E. Batson, G. Gupta, A. D. Mohite, L. Dong, D. Er, V. B. Shenoy, T. Asefa and M. Chhowalla, *Nat. Mater.*, 2016, **15**, 1003–1009.

31 X. Wu, H. Zhang, J. Zhang and X. W. Lou, *Adv. Mater.*, 2021, **33**, 2008376.

32 H. Li, C. Tsai, A. L. Koh, L. Cai, A. W. Contryman, A. H. Fragapane, J. Zhao, H. S. Han, H. C. Manoharan, F. Abild-Pedersen, J. K. Nørskov and X. Zheng, *Nat. Mater.*, 2016, **15**, 48–53.

33 Y. He, P. Tang, Z. Hu, Q. He, C. Zhu, L. Wang, Q. Zeng, P. Golani, G. Gao, W. Fu, Z. Huang, C. Gao, J. Xia, X. Wang, X. Wang, C. Zhu, Q. M. Ramasse, A. Zhang, B. An, Y. Zhang, S. Martí-Sánchez, J. R. Morante, L. Wang, B. K. Tay, B. I. Yakobson, A. Trampert, H. Zhang, M. Wu, Q. J. Wang, J. Arbiol and Z. Liu, *Nat. Commun.*, 2020, **11**, 57.

34 D. Voiry, J. Yang and M. Chhowalla, *Adv. Mater.*, 2016, **28**, 6197–6206.

35 Q. Fu, J. Han, X. Wang, P. Xu, T. Yao, J. Zhong, W. Zhong, S. Liu, T. Gao, Z. Zhang, L. Xu and B. Song, *Adv. Mater.*, 2021, **33**, 1907818.

36 J. Yao, W. Huang, W. Fang, M. Kuang, N. Jia, H. Ren, D. Liu, C. Lv, C. Liu, J. Xu and Q. Yan, *Small Methods*, 2020, **4**, 2000494.

37 L. Lin, P. Sherrell, Y. Liu, W. Lei, S. Zhang, H. Zhang, G. G. Wallace and J. Chen, *Adv. Energy Mater.*, 2020, **10**, 1903870.

38 X. Wang, Y. Zhang, J. Wu, Z. Zhang, Q. Liao, Z. Kang and Y. Zhang, *Chem. Rev.*, 2022, **122**, 1273–1348.

39 Y. Cao, *ACS Nano*, 2021, **15**, 11014–11039.

40 G. Li, Z. Chen, Y. Li, D. Zhang, W. Yang, Y. Liu and L. Cao, *ACS Nano*, 2020, **14**, 1707–1714.

41 L. Wu, A. J. F. van Hoof, N. Y. Dzade, L. Gao, M.-I. Richard, H. Friedrich, N. H. De Leeuw, E. J. M. Hensen and J. P. Hofmann, *Phys. Chem. Chem. Phys.*, 2019, **21**, 6071–6079.

42 D. Voiry, H. Yamaguchi, J. Li, R. Silva, D. C. B. Alves, T. Fujita, M. Chen, T. Asefa, V. B. Shenoy, G. Eda and M. Chhowalla, *Nat. Mater.*, 2013, **12**, 850–855.

43 A. Han, X. Zhou, X. Wang, S. Liu, Q. Xiong, Q. Zhang, L. Gu, Z. Zhuang, W. Zhang, F. Li, D. Wang, L.-J. Li and Y. Li, *Nat. Commun.*, 2021, **12**, 709.

44 D. Er, H. Ye, N. C. Frey, H. Kumar, J. Lou and V. B. Shenoy, *Nano Lett.*, 2018, **18**, 3943–3949.

45 Z. Wang, H.-H. Wu, Q. Li, F. Besenbacher, Y. Li, X. C. Zeng and M. Dong, *Adv. Sci.*, 2020, **7**, 1901382.

46 J. K. Noerskov, T. Bligaard, A. Logadottir, J. R. Kitchin, J. G. Chen, S. Pandelov and U. Stimming, *J. Electrochem. Soc.*, 2005, **152**, J23.

47 Y. Jiao, Y. Zheng, K. Davey and S.-Z. Qiao, *Nat. Energy*, 2016, **1**, 16130.

48 J. Greeley, T. F. Jaramillo, J. Bonde, I. Chorkendorff and J. K. Nørskov, *Nat. Mater.*, 2006, **5**, 909–913.

49 C. G. Morales-Guio, L.-A. Stern and X. Hu, *Chem. Soc. Rev.*, 2014, **43**, 6555–6569.

50 S. Anantharaj, S. Noda, V. R. Jothi, S. Yi, M. Driess and P. W. Menezes, *Angew. Chem., Int. Ed.*, 2021, **60**, 18981–19006.

51 C. Hu, L. Zhang and J. Gong, *Energy Environ. Sci.*, 2019, **12**, 2620–2645.

52 A. N. Enyashin, L. Yadgarov, L. Houben, I. Popov, M. Weidenbach, R. Tenne, M. Bar-Sadan and G. Seifert, *J. Phys. Chem. C*, 2011, **115**, 24586–24591.

53 J. Zhu, L. Hu, P. Zhao, L. Y. S. Lee and K.-Y. Wong, *Chem. Rev.*, 2020, **120**, 851–918.

54 J. Yang, A. R. Mohmad, Y. Wang, R. Fullon, X. Song, F. Zhao, I. Bozkurt, M. Augustin, E. J. G. Santos, H. S. Shin, W. Zhang, D. Voiry, H. Y. Jeong and M. Chhowalla, *Nat. Mater.*, 2019, **18**, 1309–1314.

55 J. Deng, H. Li, J. Xiao, Y. Tu, D. Deng, H. Yang, H. Tian, J. Li, P. Ren and X. Bao, *Energy Environ. Sci.*, 2015, **8**, 1594–1601.

56 Y. Shi, Y. Zhou, D. R. Yang, W. X. Xu, C. Wang, F. B. Wang, J. J. Xu, X. H. Xia and H. Y. Chen, *J. Am. Chem. Soc.*, 2017, **139**, 15479–15485.

This journal is © The Royal Society of Chemistry 2022

J. Mater. Chem. A, 2022, **10**, 19067–19089 | **19085**

57 Y. Shi, W. M. Huang, J. Li, Y. Zhou, Z. Q. Li, Y. C. Yin and X. H. Xia, *Nat. Commun.*, 2020, **11**, 4558.

58 Y. Shi, Z. R. Ma, Y. Y. Xiao, Y. C. Yin, W. M. Huang, Z. C. Huang, Y. Z. Zheng, F. Y. Mu, R. Huang, G. Y. Shi, Y. Y. Sun, X. H. Xia and W. Chen, *Nat. Commun.*, 2021, **12**, 3021.

59 Y. Luo, S. Zhang, H. Pan, S. Xiao, Z. Guo, L. Tang, U. Khan, B. F. Ding, M. Li, Z. Cai, Y. Zhao, W. Lv, Q. Feng, X. Zou, J. Lin, H. M. Cheng and B. Liu, *ACS Nano*, 2020, **14**, 767–776.

60 Y. R. Zheng, P. Wu, M. R. Gao, X. L. Zhang, F. Y. Gao, H. X. Ju, R. Wu, Q. Gao, R. You, W. X. Huang, S. J. Liu, S. W. Hu, J. Zhu, Z. Li and S. H. Yu, *Nat. Commun.*, 2018, **9**, 2533.

61 H. Li, L. Wang, Y. Dai, Z. Pu, Z. Lao, Y. Chen, M. Wang, X. Zheng, J. Zhu, W. Zhang, R. Si, C. Ma and J. Zeng, *Nat. Nanotechnol.*, 2018, **13**, 411–417.

62 Z. Luo, Y. Ouyang, H. Zhang, M. Xiao, J. Ge, Z. Jiang, J. Wang, D. Tang, X. Cao, C. Liu and W. Xing, *Nat. Commun.*, 2018, **9**, 2120.

63 Y. Zhou, J. Zhang, E. Song, J. Lin, J. Zhou, K. Suenaga, W. Zhou, Z. Liu, J. Liu, J. Lou and H. J. Fan, *Nat. Commun.*, 2020, **11**, 2253.

64 X. Tian, D. S. Kim, S. Yang, C. J. Ciccarino, Y. Gong, Y. Yang, Y. Yang, B. Duschatko, Y. Yuan, P. M. Ajayan, J. C. Idrobo, P. Narang and J. Miao, *Nat. Mater.*, 2020, **19**, 867–873.

65 C. Tsai, K. Chan, J. K. Nørskov and F. Abild-Pedersen, *Catal. Sci. Technol.*, 2015, **5**, 246–253.

66 X. Xu, H. Xu and D. Cheng, *Nanoscale*, 2019, **11**, 20228–20237.

67 Z. Zheng, L. Yu, M. Gao, X. Chen, W. Zhou, C. Ma, L. Wu, J. Zhu, X. Meng, J. Hu, Y. Tu, S. Wu, J. Mao, Z. Tian and D. Deng, *Nat. Commun.*, 2020, **11**, 3315.

68 M. Rajapakse, B. Karki, U. O. Abu, S. Pishgar, M. R. K. Musa, S. M. S. Riyadh, M. Yu, G. Sumanasekera and J. B. Jasinski, *npj 2D Mater. Appl.*, 2021, **5**, 1.

69 D. Rhodes, S. H. Chae, R. Ribeiro-Palau and J. Hone, *Nat. Mater.*, 2019, **18**, 541–549.

70 Z. Lin, B. R. Carvalho, E. Kahn, R. Lv, R. Rao, H. Terrones, M. A. Pimenta and M. Terrones, *2D Mater.*, 2016, **3**, 022002.

71 J. Berry, S. Ristic, S. Zhou, J. Park and D. J. Srolovitz, *Nat. Commun.*, 2019, **10**, 5210.

72 P. Liu, J. Zhu, J. Zhang, P. Xi, K. Tao, D. Gao and D. Xue, *ACS Energy Lett.*, 2017, **2**, 745–752.

73 D. Gao, B. Xia, C. Zhu, Y. Du, P. Xi, D. Xue, J. Ding and J. Wang, *J. Mater. Chem. A*, 2018, **6**, 510–515.

74 S. S. Chee, H. Jang, K. Lee and M. H. Ham, *ACS Appl. Mater. Interfaces*, 2020, **12**, 31804–31809.

75 W. Xiao, P. Liu, J. Zhang, W. Song, Y. P. Feng, D. Gao and J. Ding, *Adv. Energy Mater.*, 2017, **7**, 1602086.

76 Y. Zhao, W. Wang, C. Li and L. He, *Sci. Rep.*, 2017, **7**, 17088.

77 J. Peto, T. Ollar, P. Vancso, Z. I. Popov, G. Z. Magda, G. Dobrik, C. Hwang, P. B. Sorokin and L. Tapaszto, *Nat. Chem.*, 2018, **10**, 1246–1251.

78 J. Xie, J. Zhang, S. Li, F. Grote, X. Zhang, H. Zhang, R. Wang, Y. Lei, B. Pan and Y. Xie, *J. Am. Chem. Soc.*, 2013, **135**, 17881–17888.

79 Y. Zang, S. Niu, Y. Wu, X. Zheng, J. Cai, J. Ye, Y. Xie, Y. Liu, J. Zhou, J. Zhu, X. Liu, G. Wang and Y. Qian, *Nat. Commun.*, 2019, **10**, 1217.

80 H. Cai, Y. Guo, H. Gao and W. Guo, *Nano Energy*, 2019, **56**, 33–39.

81 A. Y. Lu, H. Zhu, J. Xiao, C. P. Chuu, Y. Han, M. H. Chiu, C. C. Cheng, C. W. Yang, K. H. Wei, Y. Yang, Y. Wang, D. Sokaras, D. Nordlund, P. Yang, D. A. Muller, M. Y. Chou, X. Zhang and L. J. Li, *Nat. Nanotechnol.*, 2017, **12**, 744–749.

82 J. Zhang, S. Jia, I. Kholmanov, L. Dong, D. Er, W. Chen, H. Guo, Z. Jin, V. B. Shenoy, L. Shi and J. Lou, *ACS Nano*, 2017, **11**, 8192–8198.

83 X. Zhang, Q. Liao, Z. Kang, B. Liu, X. Liu, Y. Ou, J. Xiao, J. Du, Y. Liu, L. Gao, L. Gu, M. Hong, H. Yu, Z. Zhang, X. Duan and Y. Zhang, *Adv. Mater.*, 2021, **33**, e2007051.

84 S. K. Kaiser, Z. Chen, D. Faust Akl, S. Mitchell and J. Perez-Ramirez, *Chem. Rev.*, 2020, **120**, 11703–11809.

85 G. Li, D. Zhang, Q. Qiao, Y. Yu, D. Peterson, A. Zafar, R. Kumar, S. Curtarolo, F. Hunte, S. Shannon, Y. Zhu, W. Yang and L. Cao, *J. Am. Chem. Soc.*, 2016, **138**, 16632–16638.

86 J. Yang, Y. Wang, M. J. Lagos, V. Manichev, R. Fullon, X. Song, D. Voiry, S. Chakraborty, W. Zhang, P. E. Batson, L. Feldman, T. Gustafsson and M. Chhowalla, *ACS Nano*, 2019, **13**, 9958–9964.

87 H. Li, M. Du, M. J. Mleczko, A. L. Koh, Y. Nishi, E. Pop, A. J. Bard and X. Zheng, *J. Am. Chem. Soc.*, 2016, **138**, 5123–5129.

88 L. Li, Z. Qin, L. Ries, S. Hong, T. Michel, J. Yang, C. Salameh, M. Bechelany, P. Miele, D. Kaplan, M. Chhowalla and D. Voiry, *ACS Nano*, 2019, **13**, 6824–6834.

89 C. Tsai, H. Li, S. Park, J. Park, H. S. Han, J. K. Norskov, X. Zheng and F. Abild-Pedersen, *Nat. Commun.*, 2017, **8**, 15113.

90 X. Wang, Y. Zhang, H. Si, Q. Zhang, J. Wu, L. Gao, X. Wei, Y. Sun, Q. Liao, Z. Zhang, K. Ammarah, L. Gu, Z. Kang and Y. Zhang, *J. Am. Chem. Soc.*, 2020, **142**, 4298–4308.

91 H. Zhang and Y. Han, *Phys. Rev. X*, 2018, **8**, 041023.

92 Y. Lee, N. Ling, D. Kim, M. Zhao, Y. A. Eshete, E. Kim, S. Cho and H. Yang, *Adv. Funct. Mater.*, 2021, **32**, 2105675.

93 J. Zhu, Z.-C. Wang, H. Dai, Q. Wang, R. Yang, H. Yu, M. Liao, J. Zhang, W. Chen, Z. Wei, N. Li, L. Du, D. Shi, W. Wang, L. Zhang, Y. Jiang and G. Zhang, *Nat. Commun.*, 2019, **10**, 1348.

94 T. Kosmala, H. Coy Diaz, H.-P. Komsa, Y. Ma, A. V. Krasheninnikov, M. Batzill and S. Agnoli, *Adv. Energy Mater.*, 2018, **8**, 1800031.

95 Q. Feng, Y. Zhu, J. Hong, M. Zhang, W. Duan, N. Mao, J. Wu, H. Xu, F. Dong, F. Lin, C. Jin, C. Wang, J. Zhang and L. Xie, *Adv. Mater.*, 2014, **26**, 2648–2653.

96 J. H. Huang, K. Y. Deng, P. S. Liu, C. T. Wu, C. T. Chou, W. H. Chang, Y. J. Lee and T. H. Hou, *Adv. Mater. Interfaces*, 2017, **4**, 1700157.

97 K. Kang, K. H. Lee, Y. Han, H. Gao, S. Xie, D. A. Muller and J. Park, *Nature*, 2017, **550**, 229–233.

19086 | *J. Mater. Chem. A*, 2022, **10**, 19067–19089

This journal is © The Royal Society of Chemistry 2022

98 K. Kang, S. Xie, L. Huang, Y. Han, P. Y. Huang, K. F. Mak, C. J. Kim, D. Muller and J. Park, *Nature*, 2015, **520**, 656–660.

99 P. D. Tran, T. V. Tran, M. Orio, S. Torelli, Q. D. Truong, K. Nayuki, Y. Sasaki, S. Y. Chiam, R. Yi, I. Honma, J. Barber and V. Artero, *Nat. Mater.*, 2016, **15**, 640–646.

100 L. Chang, Z. Sun and Y. H. Hu, *Electrochem. Energy Rev.*, 2021, **4**, 194–218.

101 Y. Fang, X. Hu, W. Zhao, J. Pan, D. Wang, K. Bu, Y. Mao, S. Chu, P. Liu, T. Zhai and F. Huang, *J. Am. Chem. Soc.*, 2019, **141**, 790–793.

102 J. Zhou, J. Lin, X. Huang, Y. Zhou, Y. Chen, J. Xia, H. Wang, Y. Xie, H. Yu, J. Lei, D. Wu, F. Liu, Q. Fu, Q. Zeng, C.-H. Hsu, C. Yang, L. Lu, T. Yu, Z. Shen, H. Lin, B. I. Yakobson, Q. Liu, K. Suenaga, G. Liu and Z. Liu, *Nature*, 2018, **556**, 355–359.

103 X. Chia, A. Y. Eng, A. Ambrosi, S. M. Tan and M. Pumera, *Chem. Rev.*, 2015, **115**, 11941–11966.

104 M. Yan, X. Zhou, X. Pan, J. Wang, L. Xia, K. Yu, X. Liao, X. Xu, L. He and L. Mai, *Nano Res.*, 2018, **11**, 3205–3212.

105 L. Liu, J. Wu, L. Wu, M. Ye, X. Liu, Q. Wang, S. Hou, P. Lu, L. Sun, J. Zheng, L. Xing, L. Gu, X. Jiang, L. Xie and L. Jiao, *Nat. Mater.*, 2018, **17**, 1108–1114.

106 K. Chang, X. Hai, H. Pang, H. Zhang, L. Shi, G. Liu, H. Liu, G. Zhao, M. Li and J. Ye, *Adv. Mater.*, 2016, **28**, 10033–10041.

107 Z. Lai, Q. He, T. H. Tran, D. V. M. Repaka, D. D. Zhou, Y. Sun, S. Xi, Y. Li, A. Chaturvedi, C. Tan, B. Chen, G. H. Nam, B. Li, C. Ling, W. Zhai, Z. Shi, D. Hu, V. Sharma, Z. Hu, Y. Chen, Z. Zhang, Y. Yu, X. Renshaw Wang, R. V. Ramanujan, Y. Ma, K. Hippalgaonkar and H. Zhang, *Nat. Mater.*, 2021, **20**, 1113–1120.

108 N. H. Attanayake, A. C. Thenuwara, A. Patra, Y. V. Aulin, T. M. Tran, H. Chakraborty, E. Borguet, M. L. Klein, J. P. Perdew and D. R. Strongin, *ACS Energy Lett.*, 2018, **3**, 7–13.

109 U. J. Kim, H. Lee, W. Lee, H. Y. Jeong, H. Kim, G. H. Han, H. S. Lee, Y. Park, Y. G. Roh, Y. H. Lee, E. Lee and S. W. Hwang, *Adv. Mater.*, 2018, **30**, e1706864.

110 J. Zhu, Z. Wang, H. Yu, N. Li, J. Zhang, J. Meng, M. Liao, J. Zhao, X. Lu, L. Du, R. Yang, D. Shi, Y. Jiang and G. Zhang, *J. Am. Chem. Soc.*, 2017, **139**, 10216–10219.

111 M. A. Lukowski, A. S. Daniel, F. Meng, A. Forticaux, L. Li and S. Jin, *J. Am. Chem. Soc.*, 2013, **135**, 10274–10277.

112 W. Ding, L. Hu, J. Dai, X. Tang, R. Wei, Z. Sheng, C. Liang, D. Shao, W. Song, Q. Liu, M. Chen, X. Zhu, S. Chou, X. Zhu, Q. Chen, Y. Sun and S. X. Dou, *ACS Nano*, 2019, **13**, 1694–1702.

113 Y. Wang, J. Xiao, H. Zhu, Y. Li, Y. Alsaid, K. Y. Fong, Y. Zhou, S. Wang, W. Shi, Y. Wang, A. Zettl, E. J. Reed and X. Zhang, *Nature*, 2017, **550**, 487–491.

114 X.-L. Fan, Y. Yang, P. Xiao and W.-M. Lau, *J. Mater. Chem. A*, 2014, **2**, 20545–20551.

115 G. Abbas, Y. Li, H. Wang, W.-X. Zhang, C. Wang and H. Zhang, *Adv. Funct. Mater.*, 2020, **30**, 2000878.

116 P. Xiong, B. Sun, N. Sakai, R. Ma, T. Sasaki, S. Wang, J. Zhang and G. Wang, *Adv. Mater.*, 2020, **32**, 1902654.

117 L. J. McGilly, A. Kerelsky, N. R. Finney, K. Shapovalov, E.-M. Shih, A. Ghiotto, Y. Zeng, S. L. Moore, W. Wu, Y. Bai, K. Watanabe, T. Taniguchi, M. Stengel, L. Zhou, J. Hone, X. Zhu, D. N. Basov, C. Dean, C. E. Dreyer and A. N. Pasupathy, *Nat. Nanotechnol.*, 2020, **15**, 580–584.

118 S. Masubuchi, M. Morimoto, S. Morikawa, M. Onodera, Y. Asakawa, K. Watanabe, T. Taniguchi and T. Machida, *Nat. Commun.*, 2018, **9**, 1413.

119 Y. Liu, Y. Huang and X. Duan, *Nature*, 2019, **567**, 323–333.

120 K. Kang, K.-H. Lee, Y. Han, H. Gao, S. Xie, D. A. Muller and J. Park, *Nature*, 2017, **550**, 229–233.

121 R. D. Westover, J. Ditto, M. Falmbigl, Z. L. Hay and D. C. Johnson, *Chem. Mater.*, 2015, **27**, 6411–6417.

122 X. Duan, C. Wang, J. C. Shaw, R. Cheng, Y. Chen, H. Li, X. Wu, Y. Tang, Q. Zhang, A. Pan, J. Jiang, R. Yu, Y. Huang and X. Duan, *Nat. Nanotechnol.*, 2014, **9**, 1024–1030.

123 Z. Jiang, W. Zhou, A. Hong, M. Guo, X. Luo and C. Yuan, *ACS Energy Lett.*, 2019, **4**, 2830–2835.

124 C. Wang, Q. He, U. Halim, Y. Liu, E. Zhu, Z. Lin, H. Xiao, X. Duan, Z. Feng, R. Cheng, N. O. Weiss, G. Ye, Y. C. Huang, H. Wu, H. C. Cheng, I. Shakir, L. Liao, X. Chen, W. A. Goddard III, Y. Huang and X. Duan, *Nature*, 2018, **555**, 231–236.

125 M. S. Islam, M. Kim, X. Jin, S. M. Oh, N.-S. Lee, H. Kim and S.-J. Hwang, *ACS Energy Lett.*, 2018, **3**, 952–960.

126 L. Xie, L. Wang, W. Zhao, S. Liu, W. Huang and Q. Zhao, *Nat. Commun.*, 2021, **12**, 5070.

127 B. Zhao, Z. Wan, Y. Liu, J. Xu, X. Yang, D. Shen, Z. Zhang, C. Guo, Q. Qian, J. Li, R. Wu, Z. Lin, X. Yan, B. Li, Z. Zhang, H. Ma, B. Li, X. Chen, Y. Qiao, I. Shakir, Z. Almutairi, F. Wei, Y. Zhang, X. Pan, Y. Huang, Y. Ping, X. Duan and X. Duan, *Nature*, 2021, **591**, 385–390.

128 P. Xiong, X. Zhang, H. Wan, S. Wang, Y. Zhao, J. Zhang, D. Zhou, W. Gao, R. Ma, T. Sasaki and G. Wang, *Nano Lett.*, 2019, **19**, 4518–4526.

129 D. R. Cummins, U. Martinez, A. Sherehiy, R. Kappera, A. Martinez-Garcia, R. K. Schulze, J. Jasinski, J. Zhang, R. K. Gupta, J. Lou, M. Chhowalla, G. Sumanasekera, A. D. Mohite, M. K. Sunkara and G. Gupta, *Nat. Commun.*, 2016, **7**, 11857.

130 W. Zhang, X. Liao, X. Pan, M. Yan, Y. Li, X. Tian, Y. Zhao, L. Xu and L. Mai, *Small*, 2019, **15**, 1900964.

131 J. Wang, M. Yan, K. Zhao, X. Liao, P. Wang, X. Pan, W. Yang and L. Mai, *Adv. Mater.*, 2017, **29**, 1604464.

132 C. V. Nguyen, *Superlattices Microstruct.*, 2018, **116**, 79–87.

133 T. V. Vu, N. V. Hieu, L. T. P. Thao, N. N. Hieu, H. V. Phuc, H. D. Bui, M. Idrees, B. Amin, L. M. Duc and C. V. Nguyen, *Phys. Chem. Chem. Phys.*, 2019, **21**, 22140–22148.

134 F. L. Ling, T. W. Zhou, X. Q. Liu, W. Kang, W. Zeng, Y. X. Zhang, L. Fang, Y. Lu and M. Zhou, *Nanotechnology*, 2017, **29**, 03LT01.

135 Y. Wang, S. Udyavara, M. Neurock and C. D. Frisbie, *Nano Lett.*, 2019, **19**, 6118–6123.

136 C.-H. Kim and C. D. Frisbie, *J. Am. Chem. Soc.*, 2016, **138**, 7220–7223.

137 C. F. Gorin, E. S. Beh and M. W. Kanan, *J. Am. Chem. Soc.*, 2012, **134**, 186–189.

This journal is © The Royal Society of Chemistry 2022

J. Mater. Chem. A, 2022, **10**, 19067–19089 | **19087**

138 B. You, M. T. Tang, C. Tsai, F. Abild-Pedersen, X. Zheng and H. Li, *Adv. Mater.*, 2019, **31**, 1807001.

139 X. Meng, T. Pandey, J. Jeong, S. Fu, J. Yang, K. Chen, A. Singh, F. He, X. Xu, J. Zhou, W.-P. Hsieh, A. K. Singh, J.-F. Lin and Y. Wang, *Phys. Rev. Lett.*, 2019, **122**, 155901.

140 P. Johari and V. B. Shenoy, *ACS Nano*, 2012, **6**, 5449–5456.

141 S. Bertolazzi, J. Brivio and A. Kis, *ACS Nano*, 2011, **5**, 9703–9709.

142 S. Schnur and A. Groß, *Phys. Rev. B*, 2010, **81**, 033402.

143 Z.-J. Zhao, S. Liu, S. Zha, D. Cheng, F. Studt, G. Henkelman and J. Gong, *Nat. Rev. Mater.*, 2019, **4**, 792–804.

144 J. R. Kitchin, J. K. Nørskov, M. A. Barteau and J. G. Chen, *J. Chem. Phys.*, 2004, **120**, 10240–10246.

145 M. Luo and S. Guo, *Nat. Rev. Mater.*, 2017, **2**, 17059.

146 C. Tsai, K. Chan, J. K. Nørskov and F. Abild-Pedersen, *J. Phys. Chem. Lett.*, 2014, **5**, 3884–3889.

147 B. Shang, X. Cui, L. Jiao, K. Qi, Y. Wang, J. Fan, Y. Yue, H. Wang, Q. Bao, X. Fan, S. Wei, W. Song, Z. Cheng, S. Guo and W. Zheng, *Nano Lett.*, 2019, **19**, 2758–2764.

148 K. Qi, X. Cui, L. Gu, S. Yu, X. Fan, M. Luo, S. Xu, N. Li, L. Zheng, Q. Zhang, J. Ma, Y. Gong, F. Lv, K. Wang, H. Huang, W. Zhang, S. Guo, W. Zheng and P. Liu, *Nat. Commun.*, 2019, **10**, 5231.

149 X. Zheng, Y. Yang, B. Sun, R. Ning, J. Sui and W. Cai, *ACS Appl. Nano Mater.*, 2021, **4**, 3493–3499.

150 Y. Tan, P. Liu, L. Chen, W. Cong, Y. Ito, J. Han, X. Guo, Z. Tang, T. Fujita, A. Hirata and M. W. Chen, *Adv. Mater.*, 2014, **26**, 8023–8028.

151 K. Jiang, M. Luo, Z. Liu, M. Peng, D. Chen, Y.-R. Lu, T.-S. Chan, F. M. F. de Groot and Y. Tan, *Nat. Commun.*, 2021, **12**, 1687.

152 H. Zhu, G. Gao, M. Du, J. Zhou, K. Wang, W. Wu, X. Chen, Y. Li, P. Ma, W. Dong, F. Duan, M. Chen, G. Wu, J. Wu, H. Yang and S. Guo, *Adv. Mater.*, 2018, **30**, 1707301.

153 J. H. Lee, W. S. Jang, S. W. Han and H. K. Baik, *Langmuir*, 2014, **30**, 9866–9873.

154 H. Li, A. W. Contryman, X. Qian, S. M. Ardakani, Y. Gong, X. Wang, J. M. Weisse, C. H. Lee, J. Zhao, P. M. Ajayan, J. Li, H. C. Manoharan and X. Zheng, *Nat. Commun.*, 2015, **6**, 7381.

155 J. Yang, D. Voiry, S. J. Ahn, D. Kang, A. Y. Kim, M. Chhowalla and H. S. Shin, *Angew. Chem., Int. Ed.*, 2013, **52**, 13751–13754.

156 Q. Yu, Y. Luo, S. Qiu, Q. Li, Z. Cai, Z. Zhang, J. Liu, C. Sun and B. Liu, *ACS Nano*, 2019, **13**, 11874–11881.

157 M. Zhou, S. Bao and A. J. Bard, *J. Am. Chem. Soc.*, 2019, **141**, 7327–7332.

158 P. Wang and B. Wang, *ACS Appl. Mater. Interfaces*, 2021, **13**, 59593–59617.

159 P. Cao, J. Peng, S. Liu, Y. Cui, Y. Hu, B. Chen, J. Li and M. Zhai, *Sci. Rep.*, 2017, **7**, 16048.

160 Y. Yan, S. Xu, H. Li, N. C. S. Selvam, J. Y. Lee, H. Lee and P. J. Yoo, *Chem. Eng. J.*, 2021, **405**, 126728.

161 S. Mao, Z. Wen, S. Ci, X. Guo, K. Ostrikov and J. Chen, *Small*, 2015, **11**, 414–419.

162 L. Najafi, S. Bellani, R. Oropesa-Nuñez, A. Ansaldo, M. Prato, A. E. Del Rio Castillo and F. Bonaccorso, *Adv. Energy Mater.*, 2018, **8**, 1703212.

163 J. Yang, Y. Liu, C. Shi, J. Zhu, X. Yang, S. Liu, L. Li, Z. Xu, C. Zhang and T. Liu, *ACS Appl. Energy Mater.*, 2018, **1**, 7035–7045.

164 T. G. Kelly and J. G. Chen, *Chem. Soc. Rev.*, 2012, **41**, 8021–8034.

165 G. Li, D. Zhang, Y. Yu, S. Huang, W. Yang and L. Cao, *J. Am. Chem. Soc.*, 2017, **139**, 16194–16200.

166 C. Zhang, Y. Chen, J.-K. Huang, X. Wu, L.-J. Li, W. Yao, J. Tersoff and C.-K. Shih, *Nat. Commun.*, 2016, **7**, 10349.

167 J. R. Waldrop, R. W. Grant, S. P. Kowalczyk and E. A. Kraut, *J. Vac. Sci. Technol., A*, 1985, **3**, 835–841.

168 G. Zhao, K. Rui, S. X. Dou and W. Sun, *J. Mater. Chem. A*, 2020, **8**, 6393–6405.

169 G. Zhao, K. Rui, S. X. Dou and W. Sun, *Adv. Funct. Mater.*, 2018, **28**, 1803291.

170 G. Yang, Y. Jiao, H. Yan, Y. Xie, A. Wu, X. Dong, D. Guo, C. Tian and H. Fu, *Adv. Mater.*, 2020, **32**, 2000455.

171 L. Tao, Y. Wang, Y. Zou, N. Zhang, Y. Zhang, Y. Wu, Y. Wang, R. Chen and S. Wang, *Adv. Energy Mater.*, 2020, **10**, 1901227.

172 H. Zhang, A. W. Maijenburg, X. Li, S. L. Schweizer and R. B. Wehrspohn, *Adv. Funct. Mater.*, 2020, **30**, 2003261.

173 J. Hu, C. Zhang, L. Jiang, H. Lin, Y. An, D. Zhou, M. K. H. Leung and S. Yang, *Joule*, 2017, **1**, 383–393.

174 L. Zhang, W. Zhang, M. Wang, H. Wang, J. Zang, W. Shen, X. Huang, D. Kong, Y. Tian, T. Xu, Y. Wang and X. Li, *J. Colloid Interface Sci.*, 2022, **614**, 267–276.

175 N. P. Dileep, P. V. Sarma, R. Prasannachandran, V. Surendran and M. M. Shaijumon, *ACS Appl. Nano Mater.*, 2021, **4**, 7206–7212.

176 G. Zhao, Y. Lin, K. Rui, Q. Zhou, Y. Chen, S. X. Dou and W. Sun, *Nanoscale*, 2018, **10**, 19074–19081.

177 M.-R. Gao, J.-X. Liang, Y.-R. Zheng, Y.-F. Xu, J. Jiang, Q. Gao, J. Li and S.-H. Yu, *Nat. Commun.*, 2015, **6**, 5982.

178 X. Ma, W. Chen, Q. Li, L. Xue and C. Peng, *Energy Environ. Mater.*, 2021, **4**, 658–663.

179 C. Yang, L. Zhou, C. Wang, W. Duan, L. Zhang, F. Zhang, J. Zhang, Y. Zhen, L. Gao, F. Fu and Y. Liang, *Appl. Catal., B*, 2022, **304**, 120993.

180 D. Li, J. Lao, C. Jiang, Y. Shen, C. Luo, R. Qi, H. Lin, R. Huang, G. I. N. Waterhouse and H. Peng, *J. Catal.*, 2020, **381**, 590–598.

181 Y. Jia, Z. Wang, X.-Q. Qiao, L. Huang, S. Gan, D. Hou, J. Zhao, C. Sun and D.-S. Li, *Chem. Eng. J.*, 2021, **424**, 130368.

182 S. Chandrasekaran, N. Li, Y. Zhuang, L. Sui, Z. Xiao, D. Fan, V. Aravindan, C. Bowen, H. Lu and Y. Liu, *Chem. Eng. J.*, 2022, **431**, 134073.

183 Y. Yin, S. Wei, L. Zhang, Z. Guo, H. Huang, S. Sai, J. Wu, Y. Xu, Y. Liu, L. Zheng, X. Fan and X. Cui, *Chem. Res. Chin. Univ.*, 2020, **36**, 1122–1127.

184 Z. Cheng, Y. Xiao, W. Wu, X. Zhang, Q. Fu, Y. Zhao and L. Qu, *ACS Nano*, 2021, **15**, 11417–11427.

19088 | *J. Mater. Chem. A*, 2022, **10**, 19067–19089

This journal is © The Royal Society of Chemistry 2022

185 J. Li, W. Hong, C. Jian, Q. Cai, X. He and W. Liu, *J. Mater. Chem. A*, 2020, **8**, 6692–6698.

186 G. Li, X. Deng, P. Chen, X. Wang, J. Ma, F. Liu and S.-F. Yin, *Chem. Eng. J.*, 2022, **433**, 134505.

187 P. Wang, X. Zhang, J. Zhang, S. Wan, S. Guo, G. Lu, J. Yao and X. Huang, *Nat. Commun.*, 2017, **8**, 14580.

188 B. Zhang, J. Liu, J. Wang, Y. Ruan, X. Ji, K. Xu, C. Chen, H. Wan, L. Miao and J. Jiang, *Nano Energy*, 2017, **37**, 74–80.

189 Y. Zhou, J. V. Pondick, J. L. Silva, J. M. Woods, D. J. Hynek, G. Matthews, X. Shen, Q. Feng, W. Liu, Z. Lu, Z. Liang, B. Brena, Z. Cai, M. Wu, L. Jiao, S. Hu, H. Wang, C. M. Araujo and J. J. Cha, *Small*, 2019, **15**, 1900078.

190 L. Ge, H. Yuan, Y. Min, L. Li, S. Chen, L. Xu and W. A. Goddard, *J. Phys. Chem. Lett.*, 2020, **11**, 869–876.

191 Y. Guo, Q. Chen, A. Nie, H. Yang, W. Wang, J. Su, S. Wang, Y. Liu, S. Wang, H. Li, Z. Liu and T. Zhai, *ACS Nano*, 2020, **14**, 1635–1644.

192 Y. He, Q. He, L. Wang, C. Zhu, P. Golani, A. D. Handoko, X. Yu, C. Gao, M. Ding, X. Wang, F. Liu, Q. Zeng, P. Yu, S. Guo, B. I. Yakobson, L. Wang, Z. W. Seh, Z. Zhang, M. Wu, Q. J. Wang, H. Zhang and Z. Liu, *Nat. Mater.*, 2019, **18**, 1098–1104.

193 Y. He, L. Liu, C. Zhu, S. Guo, P. Golani, B. Koo, P. Tang, Z. Zhao, M. Xu, C. Zhu, P. Yu, X. Zhou, C. Gao, X. Wang, Z. Shi, L. Zheng, J. Yang, B. Shin, J. Arbiol, H. Duan, Y. Du, M. Heggen, R. E. Dunin-Borkowski, W. Guo, Q. J. Wang, Z. Zhang and Z. Liu, *Nat. Catal.*, 2022, **5**, 212–221.

This journal is © The Royal Society of Chemistry 2022

J. Mater. Chem. A, 2022, **10**, 19067–19089 | **19089**